Article

Physical Model for the Geometry of Actin-Based Cellular Protrusions

G. Orly,[1] M. Naoz,[1] and N. S. Gov[1,*]
[1]Department of Chemical Physics, Weizmann Institute of Science, Rehovot, Israel

ABSTRACT Actin-based cellular protrusions are a ubiquitous feature of cell morphology, e.g., filopodia and microvilli, serving a huge variety of functions. Despite this, there is still no comprehensive model for the mechanisms that determine the geometry of these protrusions. We present here a detailed computational model that addresses a combination of multiple biochemical and physical processes involved in the dynamic regulation of the shape of these protrusions. We specifically explore the role of actin polymerization in determining both the height and width of the protrusions. Furthermore, we show that our generalized model can explain multiple morphological features of these systems, and account for the effects of specific proteins and mutations.

INTRODUCTION

Cell morphology is closely related to its functionality and is determined to a large extent by the cell's actin cytoskeleton. A common morphological feature is that of cellular protrusions, which extend from the cell and are composed of parallel cross-linked actin filaments that polymerize at the protrusion's tip (1). The shape, size, dynamics, and density of such protrusions change from cell to cell and play a crucial role in a large variety of cellular processes, from cell motility, to specific cell functions (2). Therefore, understanding the mechanisms that control the morphology of cellular protrusions is an important open problem in cell biology.

Previous theoretical works have addressed different aspects of the question of how cells form and maintain such protrusions. Some works focused on the initiation stages (3–6). Others dealt with the internal dynamics of a fully formed steady-state protrusion using either fine-grained molecular-scale simulations of the protein dynamics (7–9) or a coarse-grained continuum description (10,11). Another group of models addresses the growth dynamics (12) and the shape in more details, relating the height to the width and the forces exerted on the actin bundle (13,14). These previous models provide valuable description of certain aspects of the dynamics and shapes of protrusions. Yet, a comprehensive theory for the dynamics of the shape (height and width) of such protrusions is still lacking. In this work, we attempt to provide a theoretical framework for the dynamics and steady-state shape of the protrusions in a way that treats the main forces involved, and explains the phenomena observed in filopodia, microvilli, and stereocilia. Due to the complexity of the problem, we devised a model that combines the biochemistry and physics of the membrane and actin, and takes into account a rather wide range of possibilities for growth mechanisms and their implications.

How might the cell build an actin-filled protrusion? If the support for the actin bundle is rigid, then one could simply imagine the polymerization pushing the membrane outwards until the process stalls or the actin buckles (11). However, if the support for the actin bundle (the cytoplasm) behaves as a viscous medium, the restoring force will act to push the bundle into the cytoplasm. Therefore, to maintain a protrusion, either the restoring force must be eliminated (for example by strong binding between the membrane and the actin bundle), or there must be a protrusive force that balances it. Such a protrusive force is indeed created by the treadmilling actin bundle as it pushes against the underlying viscous cytoplasm. The cytoplasm can be treated as a viscous medium because its reorganization time is measured in seconds compared to the protrusion dynamics, which occurs over minutes (or longer). In this work, we develop the model based on this polymerization-driven protrusive force in order to explain the protrusion's height. An additional protrusive force due to actin-membrane adhesion is also considered (see the Supporting Material).

The mechanisms that control the width of actin-based protrusions in cells are also not well understood, despite previous experimental (15,16) and theoretical works (17–20), which mostly dealt with the width of the actin-bundle alone. Here we present a model for dynamic width regulation, which allows us to relate observed changes in the width to changes in the protrusion height and rate of actin polymerization (21–23).

The article is organized as follows: we first describe the model for the height of the protrusion (for a given radius), followed by the model for dynamic width regulation. We then combine both parts into a comprehensive model for the protrusion geometry and compare it to the experimental observations. Note that throughout the article we wish to emphasize the generic features, thereby all the numerical calculations plotted in the figures are dimensionless.

Submitted January 28, 2014, and accepted for publication May 28, 2014.

*Correspondence: nir.gov@weizmann.ac.il

Editor: Levi Gheber.

0006-3495/14/08/0576/12 $2.00

http://dx.doi.org/10.1016/j.bpj.2014.05.040

Model of the protrusion height

Forces

We begin by listing the main forces that act within the protrusion and affect its height. The dominant protrusive force (F_a) acting on the membrane due to the polymerization of actin is assumed to arise from the friction between the flowing actin rootlet (of surface area S_c) and the cytoplasm below the protrusion (Fig. 1) (13). On the relevant timescales of the actin flow we can treat the cytoplasm as a medium with effective friction coefficient γ_c. The friction force acting to push the treadmilling actin bundle upwards is therefore proportional to the relative velocity between the actin bundle (v_a) and the treadmilling velocity of the cytoplasm (v_{cyto}, both velocities are taken as positive for actin flow away from the membrane), as

$$F_a(t) = -\gamma_c S_c(t) \times \left(v_a(t) - v_{\mathrm{cyto}}\right), \tag{1}$$

where v_{cyto} is the treadmilling velocity of the actin cytoskeleton network below the protrusion (due to polymerization and myosin-II contractility), and

$$v_a(t) = A[h(t), t] - \dot{h}(t)$$

is the treadmilling velocity of the actin inside the protrusion, which is simply the difference between the growth velocity of the protrusion height $h(t)$ and the actin polymerization rate $A[h(t), t]$. Note that the polymerization rate could possibly depend on the radius of the protrusion (13), although we do not include this effect here. We are motivated by observations in stereocilia of different heights and widths (24), suggesting that the rate of actin polymerization is more strongly dependent on the height of the protrusion than on its radius. Note that we describe in Eq. 1 the average force, neglecting stochastic effects that may become important in the limit of small numbers of actin filaments in the bundle (7,25). Below, we shall not include v_{cyto} in our model because it is a simple constant offset.

The radius $R(z,t)$ of the protrusion at a coordinate z along its length (Fig. 1)obeys the following equation (10):

$$\dot{R}(z,t) = v_a(t)\frac{\partial R(z,t)}{\partial z} - \beta(A,z,t). \tag{2}$$

Here, $\beta(A,z,t)$ is the severing rate at the bundle surface (which could, in principle, depend on A, z, t). The first term describes the convection of the bundle downwards at the treadmilling velocity v_a, while the second term describes the local severing rate. Because the filaments in the bundle are densely packed and cross-linked we assume that the severing proteins can only act on the filaments at the bundle surface. This is motivated by detailed images of the actin bundle, for example in stereocilia (24). Both A and β can depend on the concentration profile of actin regulatory proteins (10).

In addition, protrusions may interact with an external substrate or with a neighboring protrusion, and have adhesion at their tips or along their length, which adds additional forces due to binding energy (26) and friction. For simplicity we will ignore these additional possible contributions, because many protrusions do not bind to external surfaces or to neighboring protrusions, and these terms do not add any qualitatively new behavior. There is an additional protrusive force arising from tip-activated actin-membrane binding proteins (see Eqs. S23–S27 in the Supporting Material for

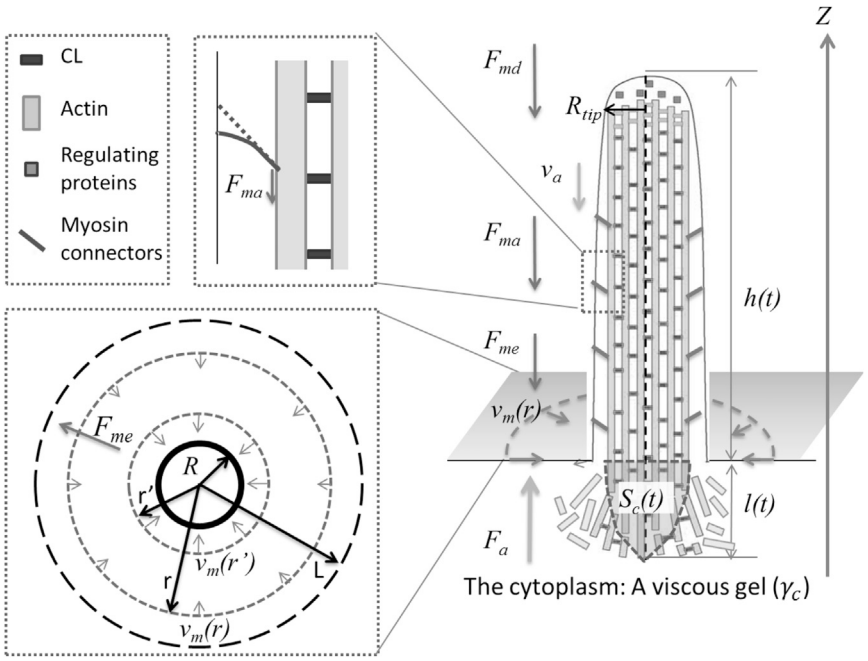

FIGURE 1 An illustration of the forces acting on the protrusion. The cytoplasm beneath the protrusion is regarded as a gel with an effective viscosity γ_c, into which the rootlet of length l and surface area S_c penetrates. The downward treadmilling velocity v_a of the rootlet in the viscous gel generates a pushing force F_a in the opposite direction. The bending and the tension elasticity of the membrane generate a restoring force F_{md}. Membrane-bound myosins connect the actin bundle to the membrane and generate an additional restoring force F_{ma}. As the protrusion elongates, the apical membrane of the cell flows toward the protrusion with velocity $v_m(r)$, generating a frictional restoring force F_{me}.

details), which for simplicity we do not include below, but which can be easily added.

Balancing these protrusive forces, there are three restoring forces exerted by the following:

1. The membrane on the actin bundle, which is due to the elastic energy of the deformed membrane (F_{md});
2. The friction between the membrane and the underlying cytoskeleton as the cellular membrane flows toward the growing protrusion (F_{me}); and
3. A force applied by actin-membrane molecular motors (F_{ma}) (Fig. 1) as the motors walk to the tip and transmit their momentum to the actin bundle.

To simplify the analysis we will neglect here the contribution of the friction force between the growing protrusion and the extracellular viscous medium, because adding this term does not qualitatively change the results.

The membrane elastic restoring force for a protrusion with local radius $R(z)$ can be written as the derivative of the Helfrich Hamiltonian with the usual membrane tension and bending (curvature) terms (27),

$$F_{md} = -\frac{\partial}{\partial h}\left(\sigma S_m + \kappa \int_0^h H(z)^2 \mathrm{d}s\right), \tag{3}$$

where σ is the effective membrane tension, κ is the effective bending modulus, S_m is the protrusion surface area, and $H(z)$ is the mean curvature at location z. For a simple cylindrical protrusion, longer than the initial tentlike shape of height h_c, this reduces to a constant value of

$$F_{md} = -(\sigma R + \kappa/R)h_c, \tag{4}$$

where h_c is the minimal height above which the membrane adopts a cylindrical shape (27). Note that curved membrane proteins, lipid composition, and passive actin-membrane binding proteins can stabilize membrane tubes by lowering the effective membrane tension and giving the membrane an effective spontaneous curvature, thereby reducing or even canceling the membrane restoring force (2) (see the Supporting Material).

The friction force F_{me} between the membrane and the underlying actin cytoskeleton around the growing protrusion (Fig. 1) can be written as (28)

$$F_{me} = -2\pi RL\tilde{\mu}\dot{h}(t) \equiv -\mu\dot{h}(t), \tag{5}$$

where $\tilde{\mu}$ is the effective friction coefficient and L is an upper cutoff length of the order of the free membrane region around the protrusion. This force arises from the flow of the membrane in the flat areas surrounding the protrusion base, toward the protrusion when its height changes. The effective friction $\tilde{\mu}$ depends on the density and strength of the anchoring sites between the surrounding membrane and the underlying cytoskeletal network.

We next describe the effects of actin-membrane connectors on the force balance. Passive connectors will reduce the effective membrane tension σ that contributes to the membrane elastic restoring force, and is therefore included in F_{md} (Eq. 4). When the connectors are composed of myosin motors they pull the membrane up the actin core, decreasing the membrane load at the tip (we assume that tip-directed motors, such as myosin-I (29), dominate). Beyond the point where the membrane tension in the protrusion is reduced to zero ($\sigma \to 0$), the motors end up adding a restoring force that pushes the actin bundle downwards. This active restoring force is linearly increasing with the total number of motors along the surface of the protrusion. For a cylindrical protrusion, we can therefore write the total restoring force acting on the actin bundle due to these motors (in the regime of local $\sigma \to 0$) as

$$F_{ma} = -2\pi R\alpha f(h(t)), \tag{6}$$

where α gives the average effective restoring force per motor and $2\pi Rf(h(t))$ is the total number of motors along the cylindrical protrusion. The function $f(h)$ is determined by the concentration profile of the motors, and for tip-directed motors (such as myosin-I and myosin-X (30)) is either a constant or a monotonously increasing function of the height (assuming no interactions between the motors).

The role of myosin-I in microvilli was investigated in McConnell and Tyska (29). When the activity of myosin-I was enhanced by exposure to ATP, the rootlets of the protrusions elongated and membrane shedding at the tips was greatly enhanced. This is attributed to myosin-I-induced forces that pull the membrane up along the actin bundle, so that excess membrane accumulates at the tips, where it is released as vesicles. This implies that myosin-I indeed applies a downward force on the actin bundle, contributing to the active restoring force F_{ma} (Eq. 6).

Combining these forces for the regime of low Reynolds number ($\ddot{h} = 0$), we extract the equation of motion for the protrusion height:

$$\dot{h} = \frac{\gamma_c S_c[h(t),t]A[h(t)] + F_{ma}[h(t)] + F_{md}[h(t)]}{\gamma_c S_c[h(t),t] + \mu}. \tag{7}$$

From this equation, we find that height dynamics is controlled by the rate of polymerization (A), the severing rate profile ($\beta(z)$), and the number of actin-membrane motors, all of which are determined by the concentration of regulating proteins in the protrusion and the availability of G-actin. We wish to examine the possible functional dependencies for these parameters on the protrusion height and width. More importantly, we search for the functional dependencies that result in a qualitative change in the solution landscape of the protrusion (i.e., under which conditions the protrusion collapses, or that several steady-state solutions appear).

The polymerization and severing rates depend on the distribution of a variety of actin-binding proteins that get transported within the protrusion. There are four basic types of transportation modes:

1. Free diffusion,
2. Binding to the actin filaments resulting in downward treadmilling velocity,
3. Binding to a myosin that walks toward the tip, or
4. Binding to myosin-VI that walks toward the base.

The resulting concentration profiles for the different transportation mechanisms were investigated in Zhuravlev and Papoian (8) and Naoz et al. (10), and are shown schematically in Fig. 2.

Polymerization rate and severing

The polymerization rate A can depend on the tip concentration of two types of proteins that either inhibit (C_i) or promote (C_p) actin polymerization (10),

$$A(h) = \frac{A_f + \Sigma_p A_f K_p C_p(h)}{1 + \Sigma_p K_p C_p(h) + \Sigma_i K_i C_i(h)} \tag{8}$$

where A_f is the free polymerization rate, A_p is the enhanced polymerization rate due to the promoter, and

$$K_l = k_{\mathrm{on},l}/k_{\mathrm{off},l}(l = i, p),$$

with k_{on} being the attachment rate and k_{off} being the detachment rate. Both A_f and A_p increase monotonously with the concentration of G-actin at the tip, up to some saturation value.

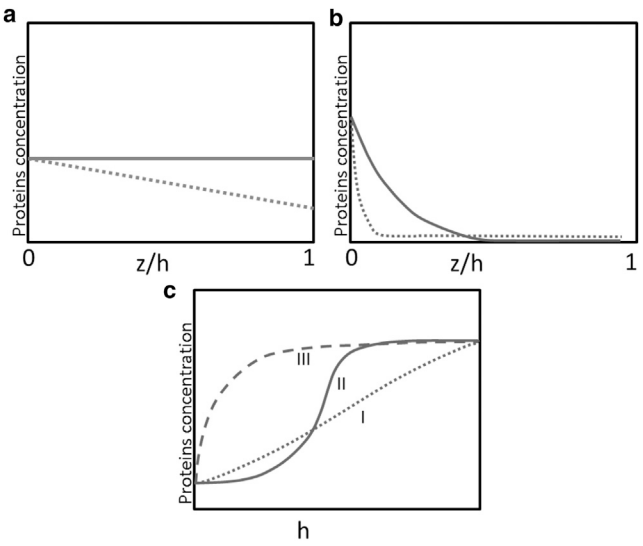

FIGURE 2 Steady-state protein concentration profiles along the protrusion (*a* and *b*) or as a function of the protrusion height h (*c*). (*a*) Simple diffusion with a sink at the tip (*dotted line*) or without it (*solid line*). (*b*) Profile of minus-end-directed myosin-VI (*solid line*) and cargo proteins that are localized to the base by binding to myosin-VI (*dotted line*). (*c*) Examples of possible concentrations of tip-directed myosins and their cargoes at the protrusion tip.

The polymerization rates A_f and A_p in general depend on a variety of factors: the availability of G-actin arriving by diffusion to the tip (7,11), active transportation of G-actin to the tip (12), load applied on the tip by the membrane (11,13), and the influx of ions into the protrusion (9,31), among others (8,10). Here we wish to explore the more general consequences of generic forms of $A(h)$, which in reality may have a complex form due to different interacting proteins that combine to affect the polymerization rate. Below, we will consider two limiting cases where $A(h)$ is either a constant (corresponding to fast diffusion, Fig. 2 *a*) or a monotonously increasing function of the height (due to tip-directed transport of regulating proteins (10), Fig. 2 *c*). We consider these two cases because it seems that G-actin availability is not limited due to diffusion along the protrusion length, as demonstrated by the growth of protrusions in a huge variety of heights (up to tens of microns in length) when the amounts of various proteins are varied (32), and by the observed increasing polymerization rate with height in stereocilia (24). These observations strongly suggest that G-actin availability by diffusion is not the limiting factor for actin polymerization in actin-based protrusions, possibly due to active transport (9,12). The case of decreasing A with h due to a reduction in the available G-actin (arriving by diffusion from the cytoplasm) is given in Eqs. S1 and S2 in the Supporting Material. Note that one can add additional mechanisms that affect $A(h)$ in this model.

Let us demonstrate an example of a tip-directed transport of a promoter of actin polymerization (consider for simplicity only one type, and no inhibitors) which results in an exponentially increasing concentration of the promoter at the tip with increasing height h (10) (see calculation given in Fig. S1). From Eq. 8, this results in an increasing function of $A(h)$ with h (see Fig. S1). Depending on the parameters, we find a sigmoidal $A(h)$ with an inflection point (see Fig. S1 and further discussion in the Supporting Material).

The severing rate of the actin filaments $\beta(z)$ is determined by the local concentration of severing proteins and by the local properties of the actin bundle such as the concentration of cross-linkers, ATP/ADP-actin content, and internal actin twist. We consider two limiting cases for the severing profile $\beta(z)$:

1. A constant severing rate along the protrusion length β_0, which corresponds to uniform distribution of the severing proteins, or
2. Severing that is entirely confined to the actin rootlet below the protrusion base, i.e., no severing at all inside the protrusion, resulting in a cylindrical shape: $R_{\mathrm{tip}} = R_{\mathrm{base}}$.

The latter case represents the limit of strong active localization of the severing proteins to the base (Fig. 2 *b*), which can

be achieved (for example) by the active transport of the severing proteins by myosin-VI motors (as was suggested to occur in stereocilia (10,33)). Deviations from a simple cylindrical shape, such as tapering of the protrusion at its base (seen in stereocilia and microvilli), do not qualitatively change the results.

Note that while actin severing always exists inside cells, there are cases where the bundle in the rootlet seems to gradually integrate into the underlying actin network, without any clear severing (34). As long as the effective protrusive forces arise in the region where the filaments spread out from the bundle and merge into the cytoplasmic network, this process can be described as an effective severing that is localized to the rootlet.

We note that the local rate of filament loss (through severing and/or depolymerization (13)) has to depend on the coordinate z along the protrusion (Eq. 2). Otherwise, the only way to maintain a steady-state height would be to perfectly match the polymerization at the tip with the depolymerization in the cytoplasm, which is a highly unstable condition.

Steady-state height of a cylindrical protrusion

We will now focus on the steady-state height and map the different regions of phase space where different behaviors can occur for a cylindrical protrusion. In the Supporting Material we present the case of uniform severing along the protrusion length, which results in a conical actin bundle and the details of the dynamics of the protrusion height.

Assuming that the density of severing proteins is constant and uniform inside the cytoplasm, the rootlet has a conical shape with area S_c (Eq. 2) given by

$$S_c(h) = \pi R_{tip}^2 \sqrt{1 + (A/\beta)^2}. \quad (9)$$

The protrusive force is now

$$F_a(h) = F_a(A(h)),$$

and therefore has the same behavior as $A(h)$ (Eq. 1), i.e.,

$$\mathrm{sign}\left[F_a'(h)\right] = \mathrm{sign}\left[A'(h)\right].$$

In Fig. 3 we plot the protrusive force for a polymerization rate that increases with the height (23) (as expected for a system where the regulating proteins are carried by tip-directed motors (10)). The membrane restoring force F_{md} (Eq. 4) for a cylindrical protrusion is independent of the height. We therefore conclude that the constant restoring force of the membrane cannot, on its own, produce a stable steady-state protrusion (Fig. 3 *a*, *dashed line*). The only solution is an unstable one, unless A is decreasing with h or the tension increases with height due to limited membrane area (35), which are both outside our regime of interest (see Eqs. S26 and S27 in the Supporting Material for the special case of the tip-activated actin-membrane binding, which can stabilize the height against a constant restoring force). Note that the constant restoring force of the membrane acts to lower the steady-state height of the protrusion, and, if it is large enough, can prevent protrusions completely (Fig. 3 *a*). Membrane tension therefore plays an important role in determining the height of protrusions.

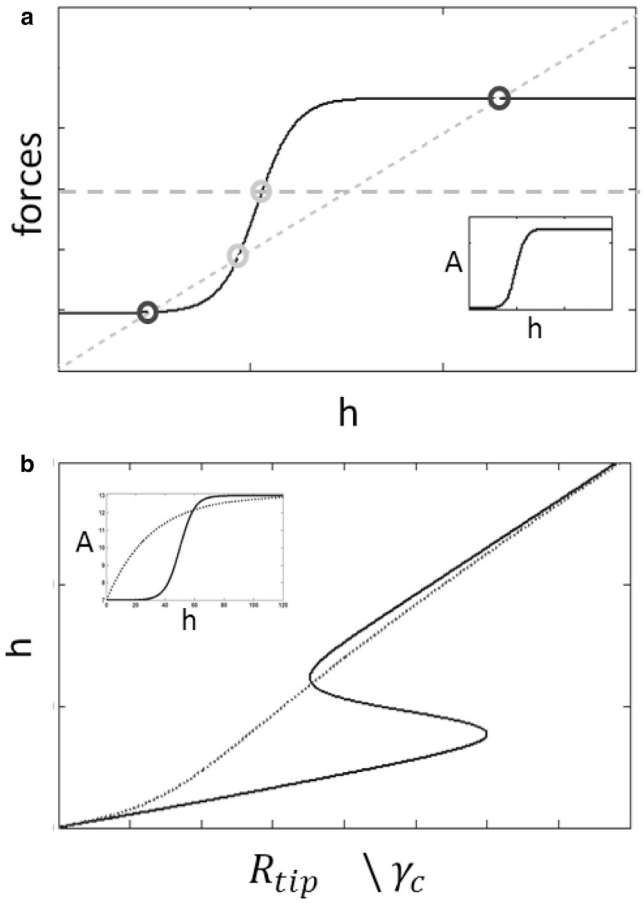

FIGURE 3 (*a*) The protrusive force $F_a(h)$ (*solid line*, and see Eq. 1) in a cylindrical protrusion has the same dependence on height h as the polymerization rate $A(h)$ (*inset*). (*Dotted line*) Restoring force due to the myosin motors $F_{ma} \propto h$ (Eq. 6); (*dashed line*) constant restoring force of the membrane F_{md} (Eq. 4). The stable (unstable) steady-state solutions (*solid* (*shaded*) *circles*). Note that the restoring force of the membrane does not provide a stable solution in this case. (*b*) The steady-state height of the cylindrical protrusion as a function of the tip complex radius R_{tip} or the cytoplasm viscosity γ_c (Eq. 10). The two line types (*solid* and *dashed*) correspond to two different functions of $A(h)$, as shown (see *inset*).

We therefore turn to the active restoring force due to actin-membrane myosins F_{ma} (Eq. 6), which increases with the height. For a uniform concentration, as is observed for the case of myosin-I (36), this force increases linearly with h. We now find that for this case (Fig. 3 *a*, *dotted line*) there exist one or two stable steady-state solutions, given by the equation (Eqs. 4, 6, and 7)

$$h_{st} = \frac{\gamma_c}{\alpha} R_{\mathrm{tip}} A \sqrt{1 + (A/\beta)^2}. \quad (10)$$

Note that when $A/\beta \gg 1$ (weak severing), the height increases quadratically with the polymerization rate ($h_{st} \propto A^2$), due to both the increase in the flow velocity of the rootlet, and its overall length. Otherwise, when severing is strong ($A/\beta \ll 1$), the relation is linear.

In general, the number of stable steady-state solution depends on the number of zeros of $A''(h)$. In Fig. 3 *b* we plot the steady-state height as a function of the protrusion radius (R_{tip}) or the cytoplasmic viscosity γ_c (Eq. 10), and demonstrate that the system can exhibit a bifurcation where h_{st} jumps discontinuously.

Protrusion width

The protrusion's radius at the tip (R_{tip}) was treated above as a free parameter. For certain types of protrusions, such as filopodia, the radius seems to have a wide distribution (33), which may result from random fluctuations in the initiation process and may not be highly regulated. However, there are examples where the width of the protrusion is highly regulated, as in the case of brush-border MV and in stereocilia. In these cases the width is uniform, with only small fluctuations between individual protrusions.

Previous models proposed to account for the radius of the protrusion through the spontaneous curvature of the tip-complex proteins (26), the elastic energy of the actin bundle (17,18), and the nucleation dynamics of the tip complex (20). However, these theories have difficulties explaining the narrow width distribution in microvilli and the observed dependence of the width on the rate of actin polymerization (21).

To account for the observations, we propose a model for the dynamical regulation of the tip-complex size. In this model, the addition and removal of new actin filaments occurs at the rim of the tip complex. Adding a new filament requires an actin nucleator (or processive-capping proteins) attached to the membrane at the tip-complex rim (at a concentration c_{nuc}), a G-actin to start the new filament (at a concentration $\rho_{\mathrm{actin}}(R_{\mathrm{tip}})$), and a free cross-linker (CL) to link the new filament to the bundle (at a concentration $\rho_{\mathrm{CL}}(R_{\mathrm{tip}})$). The nucleators get deactivated at a rate η_{nuc}, causing a removal of the nucleator and of the entire actin filament. The radius dynamics due to this process is given by

$$\dot{R}_{\mathrm{tip}} = k_{\mathrm{on}}^{\mathrm{nuc}} \rho_f(R_{\mathrm{tip}}) c_{\mathrm{nuc}} - \eta_{\mathrm{nuc}}, \quad (11)$$

where $k_{\mathrm{on}}^{\mathrm{nuc}}$ is the incorporation (and activation) rate of the nucleators at the tip complex and $\rho_f(R_{\mathrm{tip}}) = \rho_{\mathrm{actin}}(R_{\mathrm{tip}})\,\rho_{\mathrm{CL}}(R_{\mathrm{tip}})$. The steady-state radius of the tip complex is therefore given by the solution of

$$\rho_f(R_{\mathrm{tip}}) = \eta_{\mathrm{nuc}} / (k_{\mathrm{on}}^{\mathrm{nuc}} c_{\mathrm{nuc}}),$$

and it is therefore clear that a finite steady-state radius is possible only if the addition and removal of nucleators have different dependencies on R_{tip}.

Both the CL and the G-actin can reach the tip either through free diffusion or by being carried by myosin along the bundle's outer surface (7,12) (Fig. 4 *a*). Once at the tip, they diffuse from the rim of the tip complex into its center, while getting incorporated into the treadmilling bundle (Fig. 4 *b*). This process of diffusion and incorporation gives rise to a roughly exponential concentration profile for these two components, decaying from the rim inwards (Fig. 4 *c*). The length-scale that controls the exponential decay is given by

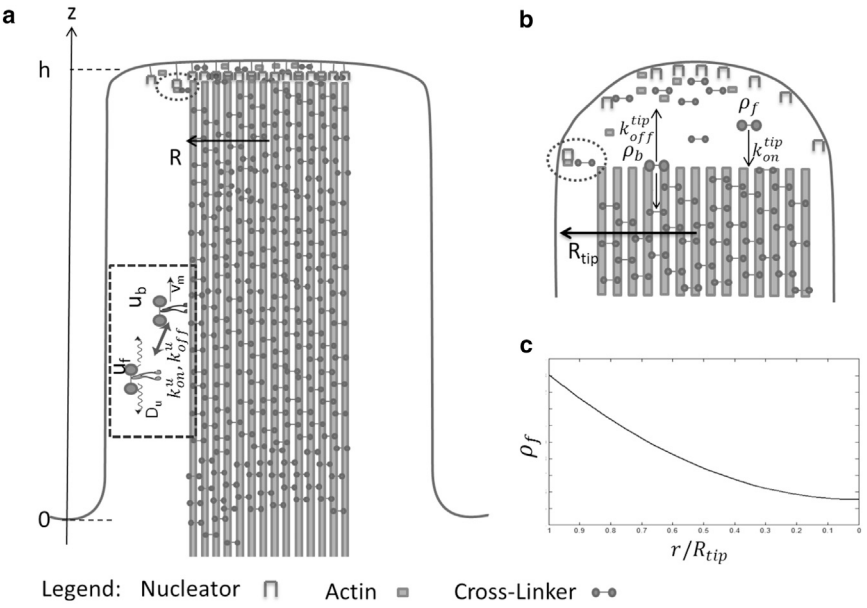

FIGURE 4 (*a*) Active transport of CL along the bundle: The myosin bound to the CL can either walk on the actin with a velocity v_m, or freely diffuse with diffusion coefficient D_u. The rates of switching between these states are k^u_{on} and k^u_{off}. Once at the tip, the CL disengages from the myosin and can diffuse along the tip complex, and be integrated into the bundle (*b*). (*c*) Resulting steady-state concentration profile of the free CL. The value $\rho_f(r)$ decays from the rim of the tip complex to the center (Eq. 18).

$$\sqrt{D_{\text{tip}}/k_{\text{tip}}},$$

where D_{tip} is the diffusion coefficient and k_{tip} is the effective incorporation rate (see below). To simplify the analysis, we will assume here that, for G-actin, this length-scale is very large, so that the distribution of G-actin across the tip-complex cross-section can be considered constant (and therefore $\rho_{\text{actin}}(R)$ is constant), and only the CL have a varying concentration profile, i.e., $\rho_f(R_{\text{tip}}) = \rho_{\text{CL}}(R_{\text{tip}})$ (the result will remain the same if we would instead assume that the G-actin profile is not constant, while the CL are uniformly distributed).

The following equations describe the CL concentration profile throughout the tip-complex cross-section (as a function of the radius $0 \le r \le R_{\text{tip}}$ in cylindrical symmetry):

$$\dot{\rho}_f(r,t) = D_{\text{tip}}\nabla_r^2\rho_f - k_{\text{on}}^{\text{tip}}\rho_f + k_{\text{off}}^{\text{tip}}\rho_b, \tag{12}$$

$$\dot{\rho}_b(r,t) = k_{\text{on}}^{\text{tip}}\rho_f(r,t) - \left(k_{\text{off}}^{\text{tip}} + A/a\right)\rho_b(r,t), \tag{13}$$

where $\rho_f(r,t)$ $\rho_b(r,t)$ are the freely diffusing and actin-bound surface concentrations of CL, $k_{\text{on}}^{\text{tip}}$ and $k_{\text{off}}^{\text{tip}}$ are the binding/unbinding rates of the CL to and from the actin, A is the polymerization velocity of the actin filaments, and a is a molecular length-scale (Fig. 4 *b*). At steady-state conditions ($\dot{\rho}_f = \dot{\rho}_b = 0$), the solution for these equations is

$$\begin{aligned}\rho_f(r) &= C(h,R_{\text{tip}})J_0\left(i\sqrt{\frac{k_{\text{tip}}}{D_{\text{tip}}}}r\right),\\ \rho_b &= \frac{a}{A}k_{\text{tip}}\rho_f,\\ k_{\text{tip}} &\equiv \frac{A}{a}\frac{k_{\text{on}}^{\text{tip}}}{k_{\text{off}}^{\text{tip}} + A/a},\end{aligned} \tag{14}$$

where J_0 is the Bessel function of the first kind. The constant C is determined by the conservation of the total number of CL

$$2\pi R(z)[J_{\text{in}}(z) - J_{\text{out}}(z)] - \frac{A}{a}\int_0^{R_{\text{tip}}} 2\pi r\rho_b(r)\mathrm{d}r = 0, \tag{15}$$

where J_{in} and J_{out} are the influx and outflux of CL, respectively, at each point along the protrusion ($0 \le z \le h$). The last term in Eq. 15 is the total flux of CL that is incorporated into the treadmilling bundle at the tip.

The fluxes J_{in} and J_{out} depend on the transportation mechanism of the CL. We will first consider the case where the CLs are carried to the protrusion tip by myosin motors. We shall assume that along the length of the protrusion the CLs are bound to the myosin motors, and can detach only at the tip. At the tip the CL cargo is released, while the myosin motor is deactivated, and is eventually recycled to the cell cytoplasm. A specific example for this scenario can be found in the myosin-III/espin-1 system (37). The motor-cargo complex can either move processively toward the plus-end with a velocity $v_m = v_w - v_a$ when actin-bound (where v_w is the processive velocity of the motor on the actin filaments), or freely diffuse with a diffusion coefficient D_u. We therefore have

$$\begin{aligned}J_{\text{in}}(z) &= v_m u_b(z),\\ J_{\text{out}}(z) &= D_u\nabla u_f(z).\end{aligned}$$

The binding and unbinding rates of the motor-cargo to the actin bundle are given by $k^u{}_{\text{on}}$ and $k^u{}_{\text{off}}$ (Fig. 4 *a*). For a cylindrical protrusions we describe this process by the following one-dimensional continuum equations (10) for the concentrations of the freely diffusing and actin-bound processive states ($u_f(z)$, $u_b(z)$),

$$\dot{u}_f = D_u\nabla_z^2 u_f + k_{\text{off}}^u u_b - k_{\text{on}}^u u_f, \tag{16}$$

$$\dot{u}_b = v_m\nabla_z u_b - k_{\text{off}}^u u_b + k_{\text{on}}^u u_f, \tag{17}$$

with boundary conditions $u_f(0) = u_0 R_{\text{base}}/R_{\text{tip}}$ (R_{base} might not be equal to R_{tip} due to tapering near the base, as in stereocilia, u_0 is the concentration of free CL+motor complexes in the cytoplasm), and $u_f(h) = \rho_f(R_{\text{tip}})$.

We assume that the dynamics of the CL transportation is much faster than the dynamics of the protrusion width changes, and therefore can use the steady-state solutions to analytically solve Eqs. 14 and 15, giving

$$\rho_f(h,R_{\text{tip}}) = \frac{u_0\frac{R_{\text{base}}}{R_{\text{tip}}}\frac{k_{\text{on}}^u}{k_{\text{off}}^u}v_m f_0}{f_1 - \frac{(z_1 - z_2)\left(f_1 k_{\text{off}}^u - f_0 k_{\text{on}}^u v_m\right)}{e^{\frac{h}{z_1}}\left(z_1 k_{\text{off}}^u + v_m\right) - e^{\frac{h}{z_2}}\left(z_2 k_{\text{off}}^u + v_m\right)}}, \tag{18}$$

where

$$\begin{aligned}z_1 &\equiv \frac{1 + \sqrt{1 + 4\frac{k_{\text{on}}^u}{D_u}\frac{v_m^2}{k_{\text{off}}^{u\,2}}}}{2\frac{k_{\text{on}}^u v_m^2}{D_u k_{\text{off}}^u}},\\ z_2 &\equiv \frac{1 - \sqrt{1 + 4\frac{k_{\text{on}}^u}{D_u}\frac{v_m^2}{k_{\text{off}}^{u\,2}}}}{2\frac{k_{\text{on}}^u v_m^2}{D_u k_{\text{off}}^u}},\\ f_0(R_{\text{tip}}) &\equiv J_0\left(i\sqrt{\frac{k_{\text{tip}}}{D_{\text{tip}}}}R_{\text{tip}}\right),\\ f_1(R_{\text{tip}}) &\equiv \sqrt{D_{\text{tip}}k_{\text{tip}}}(-i)J_1\left(i\sqrt{\frac{k_{\text{tip}}}{D_{\text{tip}}}}R_{\text{tip}}\right).\end{aligned}$$

We find from Eq. 18 that the concentration of CL at the tip increases with the height h, due to the increasing

accumulation of tip-directed motor-cargo (see Fig. S9). For long protrusions, $h \gg z_1,|z_2|$, the outflux due to diffusion at the protrusion base is effectively zero, and the CL inside the protrusion can only exit by being incorporated into the actin bundle at the tip (see Fig. S9). In this limit, $\rho_f(h,R_{\rm tip})$ reaches its maximal asymptotic value, which is independent of h:

$$\rho_0\left(h\to\infty,R_{\rm tip}\right) = \frac{f_0 v_m u_0 \frac{R_{\rm base}}{R_{\rm tip}} \frac{k^u_{\rm on}}{k^u_{\rm off}}}{f_1}. \quad (19)$$

For comparison, in the case where the CLs are transported passively by diffusion to the tip, the solution is

$$\rho_0\left(h,R_{\rm tip}\right) = \frac{f_0 u_0 \frac{R_{\rm base}}{R_{\rm tip}} D_u}{D_u f_0 + h f_1}, \quad (20)$$

and now the CL concentration at the tip decreases with h. Below we will limit the discussion to the active, myosin-driven transport of CL to the protrusion tip, which seems to be ubiquitous (for example, the myosin-III/espin-1 (37) and myosin-X/Eps8 (38) in filopodia and stereocilia).

We wish to study the tip's radius dependence on h and $A(h)$. For a fixed h, we find from Eqs. 11 and 14 that the radius decreases with increasing polymerization rate (Fig. 5 *a*), and in the limit of $R \ll \sqrt{D_{\rm tip}/k_{\rm tip}}$, $R_{\rm tip} \propto 1/k_{\rm tip}$ (Eq. 14), meaning that $R_{\rm tip} \propto 1/A$ for $A/a \ll k_{\rm off}$, and saturates for $A/a \gg k_{\rm off}$. This behavior arises due to the increased removal rate of the CLs with increasing polymerization rate, leading to a decrease in the CL concentration at the tip. Note that as A decreases the steady-state $R_{\rm tip}$ increases, until a critical value of A, where $R_{\rm tip}$ values can diverge.

For a fixed actin polymerization rate, we find that the outflux of CLs at the protrusion base increases as the height h decreases (Eq. 18), such that there is a critical height below which the steady-state solution of Eq. 11 vanishes (see Fig. S8). For long protrusions there is a constant value of CL concentration (Eq. 19), and the radius is independent of height. This behavior is shown in Fig. 5 *c*.

When the polymerization rate depends on height, the resulting dependence of the width $R_{\rm tip}$ on the height is more complicated. Let us consider that there is a promoter of actin polymerization that is carried to the tip by the same myosin motor that also carries the nucleators, or alternatively that the nucleators themselves can also act to promote a higher rate of polymerization. In both of these cases the polymerization rate can be written as

$$A(h) = \frac{A_f + A_{\rm nuc}K_{\rm nuc}c_{\rm nuc} + \sum_p A_p K_p C_p(h)}{1 + K_{\rm nuc}c_{\rm nuc} + \sum_p K_p C_p(h) + \sum_i K_i C_i(h)}, \quad (21)$$

where $K_{\rm nuc}$ and $A_{\rm nuc}$ are the effective affinity and actin polymerization rates due to the nucleator (or the protein that uses the same transport myosin). We shall consider two limiting cases:

1. The polymerization rate A does not depend on $c_{\rm nuc}$ ($A_{\rm nuc} = 0$), and
2. $c_{\rm nuc}$ is the only promoting protein effecting the polymerization rate ($K_p = K_i = 0$).

For the first case, we find as before that the radius decreases with increasing polymerization rate (Fig. 5 *a*), and therefore decreases with the height (*dashed light-shaded line* in Fig. 5 *d*). When both the nucleators' concentration ($c_{\rm nuc}$) and the polymerization rates increase with the protrusion's height h, we find that the steady-state radius can also increase with the polymerization rate (Fig. 5 *b*) and with the height (*dashed dark-shaded line* in Fig. 5 *d*).

We conclude that in the general case, the protrusion radius may increase or decrease as a function of the

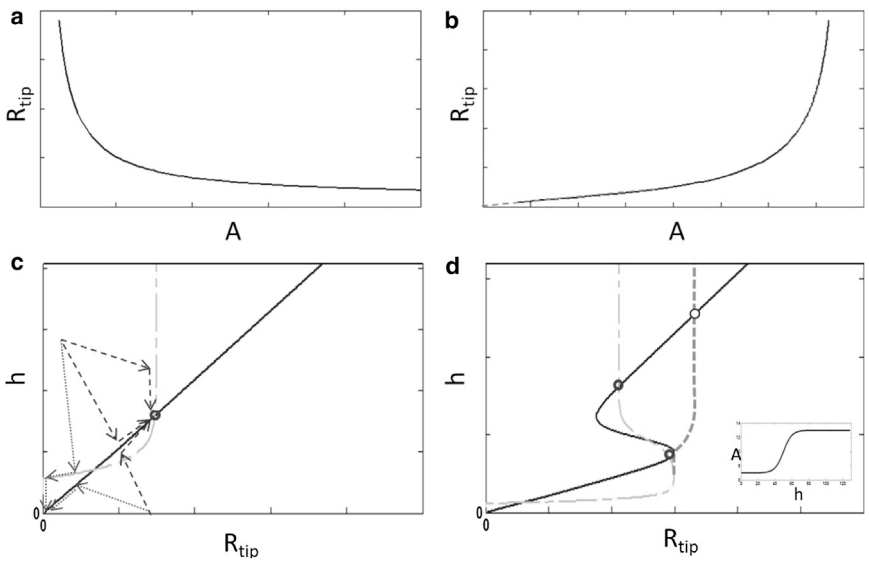

FIGURE 5 (*a*) $R_{\rm tip}$ as a function of the polymerization rate (at a fixed height), when the polymerization rate is independent of the flux of tip complex components. (*b*) As in panel *a*, when the tip complex and promoters of actin polymerization have the same transport mechanism (Eq. 21). (*c*) Steady-state height as a function of radius for a constant A (*solid line*, Eq. 10), and the steady-state protrusion radius $R_{\rm tip}$ (*gray dashed line*). (*Dashed arrows*) Possible trajectories that can lead to a stable cylindrical protrusion, or to its decay. (*d*) As in panel *c* for the case of $A(h)$ given (*inset*). (*Dashed light* (*dark*) *shaded line*) Conditions of panels *a* and *b*, respectively.

polymerization rate and the height, depending on what determines $A(h)$. This gives the cell a robust and flexible mechanism to control the relation between the protrusion's radius and height. It can also explain why in some protrusion types, such as the stereocilia, there are multiple proteins that promote actin growth and why the ratio between their concentrations may be different between different cells.

DISCUSSION

We have so far used our model to calculate the steady-state height of a cylindrical protrusion due to the force balance, and proposed a mechanism for the dynamical regulation of the tip radius (which for a cylinder is the radius of the whole protrusion). We now combine both descriptions to arrive at a model that simultaneously gives both the height and the width of cylindrical protrusions. In Fig. 5, *c* and *d*, we demonstrate that the mechanisms included in our model can allow the cell to determine the steady-state shape of cylindrical protrusions on its surface.

Note that allowing a protrusion to grow and reach the stable point indicated in Fig. 5 *c* is not trivial, and depends on the initial conditions: starting with a large tip-complex such that the stable height is reached before it disintegrates, or having a large initial tail such that the height increases fast to a large value (see below regarding filopodia dynamics and in the Supporting Material). We also see in Fig. 5 *d* that there are systems that allow for two stable solutions. These occur only when $A(h)$ has a sharp inflection point (Figs. 2 *c* and 3, and see Fig. S1 *b*), and may be reached by different initial conditions.

We now compare the model we presented above to observations of two main types of actin-driven protrusions, namely filopodia and microvilli. The specialized case of stereocilia, with its unique staircase-type organization, will be treated in a separate article.

Filopodia

We begin with the most unregulated and dynamic form of protrusion, which is observed in many cell types showing a wide distribution in length and width (39,40). These protrusions are observed to grow rapidly and then collapse, sometimes without any significant period of steady-state shape.

For the growth phase, we find that filopodia height often follows a roughly linear growth, occasionally with a pronounced overshoot (41). In our model (Eq. 7) this type of behavior can only arise if there is an initial long rootlet before the formation of the protrusion (see Fig. S2 *b*). Indeed one mechanism for the formation of filopodia involves the formation of a tight bundle of actin filaments inside the cell, before the emergence of the protrusion, as observed in detailed electron microscopy images of filopodia during their initiation stages (34). Our model relates these two observations to the same mechanism.

The collapse of the filopodia was suggested to be driven by capping events at the tip (8) and active retraction of the cytoplasmic actin network due to myosin-II contractility (42). A recent study has detailed the response of filopodia to attachment of beads at their tips, which results in filopodia retraction (43), due to a reduction in the rate of actin polymerization at the tip. In our model, the cessation of polymerization brings about a rapid collapse (see Fig. S2 *d*).

As for the overall shape of the filopodia, there are no indications that the severing proteins are actively localized along its length and therefore we may assume that they are evenly distributed along the filopodia. For uniform severing, our model predicts that the steady-state shape of the filopodia should be conical. In Yang et al. (44) there are static high -resolution images of the actin cores of filopodia, which indicate that the filopodia are indeed widest at their tips and shrink in radius toward their base. They are, however, mostly not in the shape of a simple cone—which is not surprising because these are not steady-state shapes, either growing or retracting. Similar noncylindrical shapes of filopodia are reported in Sinnar et al. (45). We further discuss the filopodia shapes in the Supporting Material.

In Zidovska and Sackmann (40) the forces induced by the elongation of filopodia were studied, and their results support some assumptions and conclusions of our model. Applying a pulling force at the filopodia tip was observed not to increase the rate of polymerization, which is in line with our assumption that the pressure of the membrane on the tip-complex is not dominant in controlling the polymerization rate. The filopodia were observed to relax nearly completely to their original lengths after switching off the external force, suggesting the existence of a steady-state length, as our model predicts. Manipulations that are likely to reduce the polymerization rate, such as by Ca^{2+} chelation or binding a bead to the filopodia tip, result in filopodia shortening, as expected by our model.

Microvilli

The category of protrusions named microvilli (MV) covers a wide range of protrusions ranging from structures that are highly dynamic and have a lifetime of several minutes (46) to structures that are stable and are highly regulated such as those appearing in brush-border cells (47). MV have, in general, a more uniform cylindrical shape than filopodia and contain a different combination of proteins. We wish to focus our discussion on MV that have a highly regulated, well-defined steady-state shape.

The cylindrical shape of the MV suggests that the severing in these systems is confined to the base due to active transport of the severing proteins, which is plausible because myosin-VI is present in these structures (48).

Indeed as expected (10), in some cases a small narrowing (tapering) at the MV base is observed. This is also equivalent in our description to the case where the actin filaments spread out from the rootlet and integrate into the cytoplasmic network.

We now compare our model to several observations regarding the steady-state shapes of MV in response to different manipulations of the cell. In Sumigray and Lechler (49), it was observed that MV are distinctly shorter when structural components of the cytoplasmic meshwork, such as keratin filaments, are depleted. Our model rationalizes these observations through a decrease of the effective cytoplasmic viscosity factor γ_c in Eq. 10.

In Zwaenepoel et al. (21), the activity of two forms of Eps8 was investigated; one form (Eps8L1a) is mainly a capping protein, while the other (Eps8) is a CL. Both proteins are actively transported to the tips of MV by myosin-XV (38). It was observed that overexpression of Eps8L1a resulted in a very large reduction in height (a factor of ~2–5), accompanied by a small increase in width of ~10%. The effect of capping proteins at the tip is to decrease the actin polymerization rate, which in our model results in a direct reduction in the height (Eq. 10). The radius in our dynamical regulation model indeed increases with decreasing polymerization rate (Fig. 5 *a*). The small observed increase may be due to the regime where the radius is weakly dependent on A ($A/a \gg k_{\mathrm{off}}$). The qualitative changes in both height and width due to changes in the rate of actin polymerization are shown in Fig. 6. When Eps8L1a was depleted, the MV grew to a larger height, while the radius decreased. Again, this fits with our interpretation that the Eps8L1a's capping activity mainly affects the polymerization rate.

The role of CL in the MV was investigated in Revenu et al. (50). It was found that the reduction of the overall cellular amount of CL resulted in thinner (by factor of ~1.4) and shorter (by factor of ~1.7) MV. From our relation between the height and the radius of cylindrical protrusions we expect a simple linear relation (Eq. 10): $h \propto R_{\mathrm{tip}}$ (assuming that the polymerization rate is independent of the height). The observed changes in the radius and height are therefore roughly consistent with this linear relation. According to our model for dynamical width regulation, indeed we expect that reducing the concentration of CL will result in a thinner tip complex (u_0 in Eqs. 11 and 18). MV with reduced CL also have shorter rootlets, which is what we expect because the rootlet length depends linearly on the radius in our model:

$$L_{\mathrm{root}} = R_{\mathrm{tip}} A/\beta. \tag{22}$$

Note that the proteins knocked-out in these experiments (such as villin) have many functions in addition to their cross-linking property, which complicates the comparison to a simple model.

Proteins that connect the actin core to the membrane, such the ERM-family, play a role by inducing an additional protrusive force (see Eq. S23 in the Supporting Material for details). Reduction in the overall concentration of such proteins results in a lower contribution of this protrusive force, and therefore shorter microvilli, as observed in experiments (1,21,51). Because such passive linkers are naturally swept away from the protrusion due to the treadmilling actin, special mechanisms can be used to maintain them along the protrusion length, such as active transport and activation at the tip (52).

In Gorelik et al. (46), the growth phase of MV follows a simple exponential form as arises in our model (see Fig. S2 *a*), for a simple restoring force that increases linearly with the height and a constant rate of polymerization. In this experiment, the collapse after termination of polymerization using application of a drug seems to be rather linear, in agreement with our model (see Fig. S2 *d*).

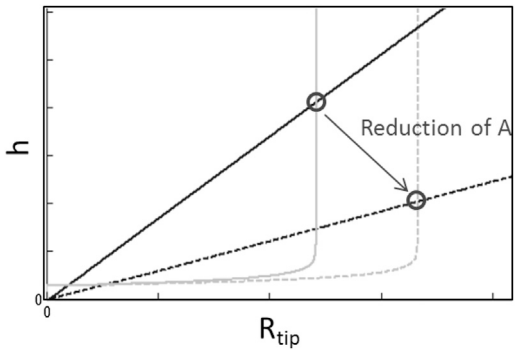

FIGURE 6 Calculated changes to the steady-state radius (R_{tip}, *shaded line*) and height (h_{st}, *solid line*, Eq. 10) of a cylindrical protrusion due to changes in the overall actin polymerization rate (*dashed lines*). Reduction of the polymerization rate can result in a proportionately larger decrease in the height compared to the change in radius, similar to what was observed in Zwaenepoel et al. (21).

CONCLUSIONS

Despite the huge complexity of cellular protrusions, the experimental data point to a direct relation between the resulting shape (height and width) and the rate of actin polymerization and availability of CL. We have presented here a model that unifies biochemical and physical processes involved in the shaping of actin-based cellular protrusions, and which, for the first time to our knowledge, can provide a theoretical framework to explain the different observations.

The model also makes predictions about the underlying processes involved in protrusion formation, which could be used to guide future experiments. For example, our model predicts that actin protrusion lengths should increase with the viscosity of the underlying cytoplasmic network. Our model also predicts that myosin motors that couple the membrane to the actin bundle (e.g., myosin-I) play a

crucial role in determining a steady-state height, by inducing a restoring force that balances the protrusive force of actin polymerization.

Our dynamic-width regulation model relates, for the first time to our knowledge, the tip-complex radius to the polymerization rate. This allows us to explain puzzling experimental observations, and provides a mechanism for cellular control over both height and width of protrusions. In addition, our model describes the dynamics of protrusion growth and collapse, including the experimentally observed over-shoot phenomenon.

Our model, as presented here, deals with individual protrusions, but can be extended to include the additional interaction forces between closely-packed protrusions (26), such as in brush-border MV (47) and stereocilia (54). The basic force balance that allows for a single protrusion to exist still needs to prevail as described in our model.

For quantitative testing of this model we would need to have information about the exact components, which does not exist at present. We therefore refrained from attempting to provide an exact quantitative fit to the observations. However, the model provides a framework with which to analyze the roles of different proteins inside such protrusions, which is otherwise difficult to extract from the experimental data.

SUPPORTING MATERIAL

Supporting Materials and Methods, 31 equations, 11 figures, and one table are available at http://www.biophysj.org/biophysj/supplemental/S0006-3495(14)00609-2.

N.S.G. gratefully acknowledges funding from the ISF (grant no. 580/12). This research is made possible in part by the historic generosity of the Harold Perlman Family. G.O. gratefully acknowledges the help of Urska Jelercic in improving the manuscript and the help of Urska Jelercic, Itai Pinkoviezki, and Abhijit Ghosh for their helpful remarks.

REFERENCES

1. Revenu, C., R. Athman, …, D. Louvard. 2004. The co-workers of actin filaments: from cell structures to signals. *Nat. Rev. Mol. Cell Biol.* 5:635–646.
2. Mattila, P. K., and P. Lappalainen. 2008. Filopodia: molecular architecture and cellular functions. *Nat. Rev. Mol. Cell Biol.* 9:446–454.
3. Gov, N. S., and A. Gopinathan. 2006. Dynamics of membranes driven by actin polymerization. *Biophys. J.* 90:454–469.
4. Veksler, A., and N. S. Gov. 2007. Phase transitions of the coupled membrane-cytoskeleton modify cellular shape. *Biophys. J.* 93:3798–3810.
5. Vaggi, F., A. Disanza, …, A. Ciliberto. 2011. The Eps8/IRSp53/VASP network differentially controls actin capping and bundling in filopodia formation. *PLOS Comput. Biol.* 7:e1002088.
6. Svitkina, T. M. 2013. Ultrastructure of protrusive actin filament arrays. *Curr. Opin. Cell Biol.* 25:574–581.
7. Lan, Y., and G. A. Papoian. 2008. The stochastic dynamics of filopodial growth. *Biophys. J.* 94:3839–3852.
8. Zhuravlev, P. I., and G. A. Papoian. 2009. Molecular noise of capping protein binding induces macroscopic instability in filopodial dynamics. *Proc. Natl. Acad. Sci. USA.* 106:11570–11575.
9. Zhuravlev, P. I., Y. Lan, …, G. A. Papoian. 2012. Theory of active transport in filopodia and stereocilia. *Proc. Natl. Acad. Sci. USA.* 109:10849–10854.
10. Naoz, M., U. Manor, …, N. S. Gov. 2008. Protein localization by actin treadmilling and molecular motors regulates stereocilia shape and treadmilling rate. *Biophys. J.* 95:5706–5718.
11. Mogilner, A., and B. Rubinstein. 2005. The physics of filopodial protrusion. *Biophys. J.* 89:782–795.
12. Zhuravlev, P. I., B. S. Der, and G. A. Papoian. 2010. Design of active transport must be highly intricate: a possible role of myosin and Ena/VASP for G-actin transport in filopodia. *Biophys. J.* 98:1439–1448.
13. Prost, J., C. Barbetta, and J. F. Joanny. 2007. Dynamical control of the shape and size of stereocilia and microvilli. *Biophys. J.* 93:1124–1133.
14. Lenz, M., J. Prost, and J. F. Joanny. 2010. Actin cross-linkers and the shape of stereocilia. *Biophys. J.* 99:2423–2433.
15. Shin, H., K. R. Purdy Drew, …, G. M. Grason. 2009. Cooperativity and frustration in protein-mediated parallel actin bundles. *Phys. Rev. Lett.* 103:238102.
16. Claessens, M. M., C. Semmrich, …, A. R. Bausch. 2008. Helical twist controls the thickness of F-actin bundles. *Proc. Natl. Acad. Sci. USA.* 105:8819–8822.
17. Grason, G. M., and R. F. Bruinsma. 2007. Chirality and equilibrium biopolymer bundles. *Phys. Rev. Lett.* 99:098101.
18. Gov, N. S. 2008. Packing defects and the width of biopolymer bundles. *Phys. Rev. E Stat. Nonlin. Soft Matter Phys.* 78:011916.
19. Isaac, E. B., U. Manor, …, S. Nir. 2013. Linking actin networks and cell membrane via a reaction-diffusion-elastic description of nonlinear filopodia initiation. *Phys. Rev. E.* 88:022718.
20. Haviv, L., N. Gov, …, A. Bernheim-Groswasser. 2008. Thickness distribution of actin bundles in vitro. *Eur. Biophys. J.* 37:447–454.
21. Zwaenepoel, I., A. Naba, …, M. Arpin. 2012. Ezrin regulates microvillus morphogenesis by promoting distinct activities of Eps8 proteins. *Mol. Biol. Cell.* 23:1080–1094.
22. Sekerková, G., C. P. Richter, and J. R. Bartles. 2011. Roles of the espin actin-bundling proteins in the morphogenesis and stabilization of hair cell stereocilia revealed in CBA/CaJ congenic jerker mice. *PLoS Genet.* 7:e1002032.
23. Rzadzinska, A., M. Schneider, …, B. Kachar. 2005. Balanced levels of Espin are critical for stereociliary growth and length maintenance. *Cell Motil. Cytoskeleton.* 62:157–165.
24. Rzadzinska, A. K., M. E. Schneider, …, B. Kachar. 2004. An actin molecular treadmill and myosins maintain stereocilia functional architecture and self-renewal. *J. Cell Biol.* 164:887–897.
25. Wolff, K., C. Barrett-Freeman, …, D. Marenduzzo. 2014. Modeling the effect of myosin X motors on filopodia growth. *Phys. Biol.* 11:016005.
26. Gov, N. S. 2006. Dynamics and morphology of microvilli driven by actin polymerization. *Phys. Rev. Lett.* 97:018101.
27. Derényi, I., F. Jülicher, and J. Prost. 2002. Formation and interaction of membrane tubes. *Phys. Rev. Lett.* 88:238101.
28. Brochard-Wyart, F., N. Borghi, …, P. Nassoy. 2006. Hydrodynamic narrowing of tubes extruded from cells. *Proc. Natl. Acad. Sci. USA.* 103:7660–7663.
29. McConnell, R. E., and M. J. Tyska. 2010. Leveraging the membrane - cytoskeleton interface with myosin-1. *Trends Cell Biol.* 20:418–426.
30. Sousa, A. D., and R. E. Cheney. 2005. Myosin-X: a molecular motor at the cell's fingertips. *Trends Cell Biol.* 15:533–539.
31. Revenu, C., M. Courtois, …, S. Robine. 2007. Villin severing activity enhances actin-based motility in vivo. *Mol. Biol. Cell.* 18:827–838.
32. Salles, F. T., R. C. Merritt, Jr., …, B. Kachar. 2009. Myosin IIIa boosts elongation of stereocilia by transporting espin 1 to the plus ends of actin filaments. *Nat. Cell Biol.* 11:443–450.

33. Sakaguchi, H., J. Tokita, …, B. Kachar. 2008. Dynamic compartmentalization of protein tyrosine phosphatase receptor Q at the proximal end of stereocilia: implication of myosin VI-based transport. *Cell Motil. Cytoskeleton.* 65:528–538.

34. Svitkina, T. M., E. A. Bulanova, …, G. G. Borisy. 2003. Mechanism of filopodia initiation by reorganization of a dendritic network. *J. Cell Biol.* 160:409–421.

35. Sens, P., and S. Safran. 1998. Pore formation and area exchange in tense membranes. *Europhys. Lett.* 43:95.

36. Schneider, M. E., A. C. Dosé, …, B. Kachar. 2006. A new compartment at stereocilia tips defined by spatial and temporal patterns of myosin IIIa expression. *J. Neurosci.* 26:10243–10252.

37. Quintero, O. A., W. C. Unrath, …, C. M. Yengo. 2013. Myosin 3A kinase activity is regulated by phosphorylation of the kinase domain activation loop. *J. Biol. Chem.* 288:37126–37137.

38. Manor, U., A. Disanza, …, B. Kachar. 2011. Regulation of stereocilia length by myosin XVa and whirlin depends on the actin-regulatory protein Eps8. *Curr. Biol.* 21:167–172.

39. Lee, K. C., A. Gopinathan, and J. M. Schwarz. 2011. Modeling the formation of in vitro filopodia. *J. Math. Biol.* 63:229–261.

40. Zidovska, A., and E. Sackmann. 2011. On the mechanical stabilization of filopodia. *Biophys. J.* 100:1428–1437.

41. Watanabe, T. M., H. Tokuo, …, M. Ikebe. 2010. Myosin-X induces filopodia by multiple elongation mechanism. *J. Biol. Chem.* 285: 19605–19614.

42. Mallavarapu, A., and T. Mitchison. 1999. Regulated actin cytoskeleton assembly at filopodium tips controls their extension and retraction. *J. Cell Biol.* 146:1097–1106.

43. Bornschlgl, A. T. 2013. Filopodial retraction force is generated by cortical actin dynamics and controlled by reversible tethering at the tip. *Proc. Natl. Acad. Sci. USA.* 110:18928–18933.

44. Yang, C., L. Czech, …, T. Svitkina. 2007. Novel roles of formin mDia2 in lamellipodia and filopodia formation in motile cells. *PLoS Biol.* 5:e317.

45. Sinnar, S. A., S. Antoku, …, S. Halpain. 2014. Capping protein is essential for cell migration in vivo and for filopodial morphology and dynamics. *Mol. Biol. Cell.*: 2014 May 14. pii: mbc.E13-12-0749. [Epub ahead of print].

46. Gorelik, J., A. I. Shevchuk, …, Y. E. Korchev. 2003. Dynamic assembly of surface structures in living cells. *Proc. Natl. Acad. Sci. USA.* 100:5819–5822.

47. Mooseker, M. S. 1985. Organization, chemistry, and assembly of the cytoskeletal apparatus of the intestinal brush border. *Annu. Rev. Cell Biol.* 1:209–241.

48. Hegan, P., H. Giral, …, M. Mooseker. 2012. Myosin VI is required for maintenance of brush border structure, composition, and membrane trafficking functions in the intestinal epithelial cell. *Cytoskeleton*.

49. Sumigray, K. D., and T. Lechler. 2012. Desmoplakin controls microvilli length but not cell adhesion or keratin organization in the intestinal epithelium. *Mol. Biol. Cell.* 23:792–799.

50. Revenu, C., F. Ubelmann, …, S. Robine. 2012. A new role for the architecture of microvillar actin bundles in apical retention of membrane proteins. *Mol. Biol. Cell.* 23:324–336.

51. Yonemura, S., S. Tsukita, and S. Tsukita. 1999. Direct involvement of ezrin/radixin/moesin (ERM)-binding membrane proteins in the organization of microvilli in collaboration with activated ERM proteins. *J. Cell Biol.* 145:1497–1509.

52. Viswanatha, R., A. Bretscher, and D. Garbett. 2014. Dynamics of ezrin and EBP50 in regulating microvilli on the apical aspect of epithelial cells. *Biochem. Soc. Trans.* 42:189–194.

53. Reference deleted in proof.

54. Müller, U. 2008. Cadherins and mechanotransduction by hair cells. *Curr. Opin. Cell Biol.* 20:557–566.

Supplementary Material: Physical model for the geometry of actin-based cellular protrusions

G. Orly, M. Naoz and and N. S. Gov*
Department of Chemical Physics, The Weizmann Institute of Science, P.O. Box 26, Rehovot, Israel 76100

PACS numbers:

POLYMERIZATION RATE DECREASING WITH HEIGHT

When the actin polymerization at the tip is limited by the supply of G-actin that is transported by diffusion from the cytoplasm (protrusion base), we get that

$$A = A_0 \frac{1}{1 + h/h_D} \tag{S1}$$

where A_0 is the polymerization rate given the concentration of G-monomers at the protrusion base, $h_D = D * k_{on}/\delta$, where D is the diffusion coefficient of the G-actin along the protrusion, k_{on} is the rate of incorporation per G-actin at the tip and δ is the size of a monomer.

Under these conditions, a steady-state height of a cylindrical protrusion is possible even for a constant restoring force of a tubular membrane (Eq.4). The steady-state height, instead of Eq.(10) is now given by (assuming we are dominated by tension in Eq.4)

$$h_{st} = \frac{\sqrt{2}\sqrt{A_0^2\beta\gamma_c h_c^2 h_d^2 R\sigma^2\left(\sqrt{4h_c^2\sigma^2 + \beta^2\gamma_c^2 R^2} + \beta\gamma_c R\right)} - 2\beta h_c^2 h_d \sigma^2}{2\beta h_c^2 \sigma^2} \tag{S2}$$

For $R \ll 2h_c\sigma/(\beta\gamma_c)$ the height increases as $\sqrt{R}$, and linearly with R for large R.

CALCULATION OF THE POLYMERIZATION RATE $A(h)$ FOR THE CASE OF A TIP-TRANSPORTED PROMOTER

Let us demonstrate an example of an explicit calculation of $A(h)$ for the case of a single type of promoter of actin polymerization that is carried to the tip by a myosin motor. We consider that the cargo protein plus its carrying motor form a single complex (for simplicity), which can either move processively to the tip at the velocity $v_m = v_w - v_a$ (where v_w is the processive velocity of the motor on the actin filaments), or detach from the actin and diffuse freely in the protrusion with diffusion coefficient D. This is identical to the case treated in [1] and the equations are the same as Eqs.16,17

$$\dot{\rho_f} = D\nabla_z^2\rho_f + k_{off}\rho_b - k_{on}\rho_f \tag{S3}$$

$$\dot{\rho_b} = v_m\nabla_z\rho_b - k_{off}\rho_b + k_{on}\rho_f \tag{S4}$$

The resulting distribution of the free and actin-bound complexes along the length of the protrusion are given by [1]

$$\begin{aligned}\rho_f(z) &= \frac{1}{2\sqrt{D}\left(Dk_{off}^2+4k_{on}v_m^2\right)}\Big[\exp\left(\frac{x\left(\sqrt{D}k_{off}-\sqrt{Dk_{off}^2+4k_{on}v_m^2}\right)}{2\sqrt{D}v_m}\right)\\ &\left(D^{3/2}k_{off}^2\rho_{f,0}\left(e^{\frac{x\sqrt{Dk_{off}^2+4k_{on}v_m^2}}{\sqrt{D}v_m}}+1\right)\right.\\ &-Dk_{off}\rho_{f,0}\sqrt{Dk_{off}^2+4k_{on}v_m^2}\left(e^{\frac{x\sqrt{Dk_{off}^2+4k_{on}v_m^2}}{\sqrt{D}v_m}}-1\right)\\ &+4\sqrt{D}k_{on}\rho_{f,0}v_m^2\left(e^{\frac{x\sqrt{Dk_{off}^2+4k_{on}v_m^2}}{\sqrt{D}v_m}}+1\right)\\ &\left.-2\rho_{b,0}v_m^2\sqrt{Dk_{off}^2+4k_{on}v_m^2}\left(e^{\frac{x\sqrt{Dk_{off}^2+4k_{on}v_m^2}}{\sqrt{D}v_m}}-1\right)2\sqrt{D}\left(Dk_{off}^2+4k_{on}v_m^2\right)\right)\Big]\end{aligned} \tag{S5}$$

$$\begin{aligned}\rho_b(z) &= \frac{1}{2\left(Dk_{off}^2+4k_{on}v_m^2\right)}\Big[\exp\left(\frac{x\left(\sqrt{D}k_{off}-\sqrt{Dk_{off}^2+4k_{on}v_m^2}\right)}{2\sqrt{D}v_m}\right)\\ &\left(\sqrt{D}(k_{off}\rho_{b,0}-2k_{on}\rho_{f,0})\sqrt{Dk_{off}^2+4k_{on}v_m^2}\left(e^{\frac{x\sqrt{Dk_{off}^2+4k_{on}v_m^2}}{\sqrt{D}v_m}}-1\right)\right.\\ &\left.+Dk_{off}^2\rho_{b,0}\left(e^{\frac{x\sqrt{Dk_{off}^2+4k_{on}v_m^2}}{\sqrt{D}v_m}}+1\right)+4k_{on}\rho_{b,0}v_m^2\left(e^{\frac{x\sqrt{Dk_{off}^2+4k_{on}v_m^2}}{\sqrt{D}v_m}}+1\right)\right)\Big]\end{aligned} \tag{S6}$$

where k_{on}, k_{off} are the on/off rates from the actin-bound to free states, and $\rho_{f,0}, \rho_{b,0}$ are the concentrations of the free and actin-bound complexes at the protrusion base (cytoplasm). We plot this distribution in Fig.S1a.

Using the concentration of free promoter at the tip $\rho_f(h) = C_p(h)$ from Eq.S5 in Eq.8 (assuming that the free promoter is available to interact at the tip and affect the polymerization rate), we get $A(h)$

$$A(h) = \frac{A_f + A_p K_p C_p(h)}{1 + K_p C_p(h)} \tag{S7}$$

In Fig.S1b we plot the result of Eq.S7 for various parameters.

We can get an estimate of the height h at which $A(h)$ has an inflection point, by noting that usually $v_w \gg v_a$ and solving for the height at which $1 = K_p C_p(h)$. We get

$$\begin{aligned}h_{inflection} &\simeq \frac{2\sqrt{D}v_m}{\sqrt{D}k_{off}-\sqrt{Dk_{off}^2+4k_{on}v_m^2}}\\ &\log\left(\frac{2\sqrt{D}\left(Dk_{off}^2+4k_{on}v_m^2\right)}{K_p\left(D^{3/2}k_{off}^2\rho_{f,0}+Dk_{off}\rho_{f,0}\sqrt{Dk_{off}^2+4k_{on}v_m^2}+2\rho_{b,0}v_m^2\sqrt{Dk_{off}^2+4k_{on}v_m^2}+4\sqrt{D}k_{on}\rho_{f,0}v_m^2\right)}\right)\end{aligned} \tag{S8}$$

This estimate is denoted by the dashed vertical lines in Fig.S1b, and gives a very good estimate of the inflection point. We find that the inflection point moves to larger heights when the motor velocity decreases (green line in Fig.S1b) or the affinity of the promoter decreases (black line in Fig.S1b).

GROWTH DYNAMICS

Constant tip-complex radius

We begin this section by studying the height dynamics of the protrusion, for the case of a constant radius of the tip complex. The height dynamics of a cylindrical protrusion is presented in (Eq.7) and the numerical solution is

plotted in Fig.S2 for four representative cases: constant polymerization rate with no initial tail (Fig.S2a), constant polymerization rate with a long initial tail (Fig.S2b), polymerization rate that increases with height (Fig.S2c) and the collapse following the termination of the polymerization (Fig.S2d).

For the simple case of a cylindrical protrusion where there is a single steady-state solution and there is no extrema in the total protrusive force ($F_{tot} \equiv F_a - F_{md} - F_{ma}$, Eqs.1,3-6), and taking $\mu \sim 0$, we find that the dominant restoring force is due to $F_{ma} \propto h$. Taking a constant polymerization rate A, we can simplify (Eq.7) in the form

$$\gamma_c (A - \dot{h}) S_c = 2\alpha R_{tip} h. \tag{S9}$$

If $\dot{h}$ is small, such that the rootlet achieves a steady-state conical shape (Eq.9), we can write

$$\gamma_c R_{base}^2 \sqrt{1 + \left(\frac{A - \dot{h}}{\beta}\right)^2} (A - \dot{h}) = 2\alpha R_{tip} h. \tag{S10}$$

This equation can be solved analytically in four regimes:

When the protrusion starts growing from a very short initial tail the growth rate can be approximated by: $\dot{h} = A$. As the protrusion elongates further the growth rate decays exponentially to zero ($A \gg \dot{h}$) with time scale of

$$\tau_h = \frac{h_{st}}{A}. \tag{S11}$$

where h_{st} is the steady-state height (Eq.10).

The analytical solutions in both these limits have an initial slope of $\dot{h} = A$ which is the maximal possible growth rate (cases 1,2 in Table I). The exact numerical solution has a smaller slope since the protrusion does not just elongate at the initial stages but also forms the rootlet needed for support (Fig.S2a).

A different dynamics arises when the protrusion has a long initial rootlet, before it starts protruding from the cell, as is found experimentally in some cases [3]. We now find that the height makes an over-shoot above the steady-state height, and decays towards the steady-state value as the initial rootlet is severed (Fig.S2b). A large initial rootlet allows the protrusion to grow at a fast rate (reaching the maximal rate of $\dot{h} = A$) and therefore reach a significant height sooner. In a case where more than a single steady-state height exists, this may allow reaching higher solutions.

When $F_{tot}(h)$ has extrema, we can acquire the growth dynamics that leads to the higher branch (or branches) of steady-state solutions while the growth rate is still affected by the proximity of an additional solution (Fig.S2c). This situation can occur for example when the restoring force is simply linear with h, but the polymerization rate increases with h and has an inflexion point $A''(h) = 0$, as shown. Other possible combinations of restoring and protrusive forces can also give rise to this behavior.

To conclude, while there is polymerization we find that the height is a monotonously increasing function of time, unless there is a large initial rootlet that gives rise to an over-shoot behavior.

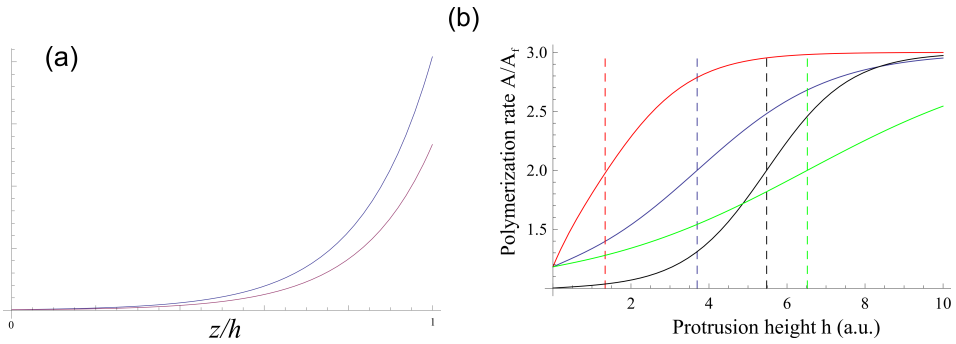

FIG. S1: (a) Concentration profiles of the myosin-plus-cargo complex along the protrusion height z, for a tip-directed transport (Eqs.S5,S6 [1]). Blue line is for the free component ρ_f, and purple for the actin-bound component ρ_b, (using the parameters (arbitrary units): $v_a = 0.1, v_w = 1, k_{on} = 1, k_{off} = 1, D = 1, \rho_{f,0} = \rho_{b,0} = 0.1$). (b) Calculation of the polymerization rate $A(h)$ as a function of the protrusion height, using Eq.S7 (Eq.8) and the distribution of the free component from Eq.S5, using $K_p = 1, A_f = 1, A_p = 3$. Blue is for the same parameters as in (a), while red is for $v_w = 5$, black is for $v_w = 10, K_p = 0.01$, and green for $v_w = 0.5, K_p = 1$. The vertical dashed lines give the estimated location of the inflection point given by $h_{inflection}$ (Eq.S8).

When the polymerization is terminated the protrusion retracts with an initial rate that is approximately constant. Only when the protrusion is small one observes slower than linear decay until the protrusion finally disappears (Fig.S2d). For the parameters taken in this example we see a good fit of the numerical solution to the case where $\dot{h} \gg \beta$ (case 3 in Table I).

Dynamics of the height and the tip complex radius combined

The dynamical width regulation mechanism for a cylindrical protrusion (Eq.21) can be written in the limit of $R_{tip} \ll \sqrt{D_{tip}/k_{tip}}$ (which as discussed below is probably the biologically relevant regime) as

$$\dot{R_{tip}} = \frac{\chi}{R_{tip}} - \eta \tag{S12}$$

where $\chi = 2J_{eff}k_{on}^{nuc}c_{nuc}/k_{tip}$ and $J_{eff} = v_m u_0 \frac{R_{base}}{R_{tip}} \frac{k_{on}^u}{k_{off}^u}$ (R_{base}/R_{tip} is a constant in a cylindrical protrusion). The solution of this equation is in the form of a Lambert W-function, which is monotonously increasing with time up to the steady-state value $R_{tip}^{st} = \chi/\eta$. The time-scale for this growth is given by

$$\tau_R = \frac{R_{tip}^{st}}{\eta}. \tag{S13}$$

In Fig.S3 we plot the calculated growth dynamics of both the tip-complex radius and protrusion height for $O(\tau_h) = O(\tau_R)$. Note that in the case where $\tau_h \ll \tau_R$ the initial radius must be large enough so that the protrusion will not disappear before reaching a sufficient length.

STEADY-STATE CONICAL PROTRUSIONS

In the case of a constant severing rate β along the protrusion the result is a conical shaped protrusion as presented in Fig.S4

We begin by analyzing the steady-state height for this geometry, for a fixed radius of the tip complex R_{tip}. The protrusive force of the actin treadmilling is $F_a = \gamma_c S_c(h) A(h)$ (Eq.1, at steady-state $\dot{h} = 0$) and the rootlet area S_c (Eq.9) is now given by

$$S_c(h) = \pi[R_{tip} - (\beta/A)h]^2 \sqrt{1 + (A/\beta)^2} \tag{S14}$$

TABLE I: Analytical expressions for the growth dynamics of different scenarios.

	case	Equation	result
1	$A \gg \dot{h}$	$\dot{h} = A - \frac{2\alpha R_{tip} h}{\gamma_c R_{base}^2 \sqrt{1+(A/\beta)^2}}$	$h(t) = h_{st}\left(1 - e^{-t/\tau_h}\right) \quad \tau_h = \frac{h_{st}}{A}$
	h_{st} is the steady-state height (Eq.10).		
2	$A \simeq \dot{h}$	$\gamma_c(A - \dot{h})S_c(0) = 2\alpha R_{tip} h$	$h(t) = A\omega(1 - e^{-t/\omega}), \quad \omega = \frac{\gamma_c S_c(0)}{2\alpha R_{tip}}$
	$S_c(0)$ is the initial rootlet. This case corresponds to the initial growth.		
3	$A = 0$, $\dot{h} \gg \beta$	$(\dot{h})^2 = \frac{2\alpha\beta R_{tip}}{\gamma_c R_{b2}} h$	$h(t) = \frac{\left(\sqrt{2\alpha\beta R_{tip}}t - 2R_{base}\sqrt{\gamma_c h_{st}}\right)^2}{4\gamma_c R_{base}^2}$
	The initial retraction stage following the termination of the polymerization.		
4	$A = 0$, $\dot{h} \ll \beta$	$\dot{h} = -\frac{2\alpha R_{tip}}{\gamma_c R_{b2}} h$	$h(t) = h_{st} e^{-t/\tilde{\omega}}, \quad \tilde{\omega} = \frac{\gamma_c R_{base}^2}{2\alpha R_{tip}}$
	The final retraction stage following the termination of the polymerization.		

where h can range between zero and the maximal height $h_{max} = R_{tip}A/\beta$, and is determined by the force balance (Eq.7). The protrusive force is monotonously decreasing with height when

$$A'(h) < \frac{\beta}{\Omega R_{tip} + (1-\Omega)(\beta/A)h}$$

where $\Omega \equiv [1+2(A/\beta)^2]/[2+2(A/\beta)^2]$, and otherwise increasing with the height, as shown in Fig.S5.

Therefore if the polymerization rate depends on the height, as was found for the case of stereocilia [2], it is possible to have an extremum (or even several extrema) in $F_a(h)$, depending on the nature of $A(h)$. As we shall see this allows the option of multiple steady-state heights.

The restoring forces applied by the membrane and the myosin motors are

$$F_{md} = 2\pi\kappa\frac{A}{\beta}\frac{1}{\sqrt{1+\left(\frac{\beta}{A}\right)^2}L_{root}} + 2\pi\sigma\frac{\beta}{A}\sqrt{1+\left(\frac{\beta}{A}\right)^2}L_{root} \tag{S15}$$

$$F_{ma} = \pi\alpha\frac{\beta}{A}\sqrt{1+\left(\frac{\beta}{A}\right)^2}\left(h^2+2hL_{root}\right) \tag{S16}$$

The results are plotted in Fig.S6 for the case of a constant polymerization rate, and for an increasing $A(h)$ as given in the inset. For a constant polymerization rate we find that there is only a single stable steady-state solution and the height grows linearly with the tip-complex radius. For the case of an increasing (steeply enough) $A(h)$ there can be additional stable steady-states heights. In general, for all realistic types of the restoring force the maximal number of stable steady-state solution is $[N/2]+1$ where N is the number of extrema of $F_a(h)$.

Note that the sharp increase in the membrane restoring force at large heights arises from the very narrow rootlet of the conical protrusion in this limit.

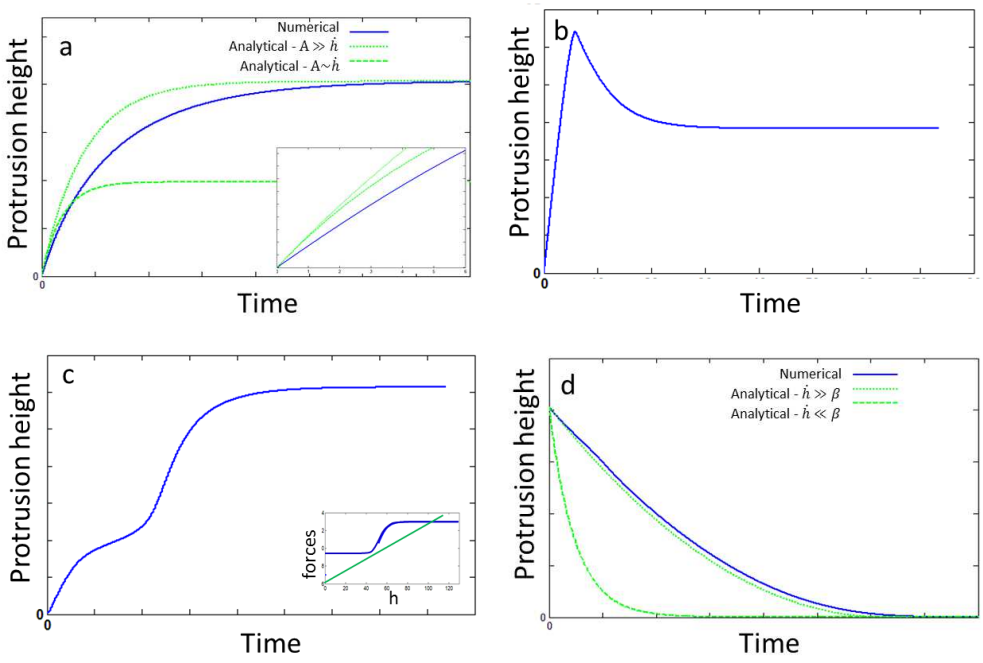

FIG. S2: The height dynamics of a cylindrical protrusion. a) A constant rate of polymerization and a monotonic restoring force with no initial tail (numerical solution in blue, analytical solutions in green: solid line case 1, dashed line case 2 in Table I). In the inset we highlight the initial growth stage showing that the real slope in smaller than A. b) Calculation with an initial long tail giving initial slope of $\dot{h} = A$ and an overshoot in the height above the steady-state value. c) The growth dynamics for the protrusive and restoring forces as shown in the inset (blue and green respectively). d) Retraction dynamics of the protrusion following the termination of the polymerization (numerical solution in blue and analytical solutions in green: solid line case 3 and dashed line case 4 of Table I).

This gives rise to a discontinuity in the steady-state height as a function of both the protrusion tip's radius R_{tip} and the cell's viscosity γ_c, as shown in Fig.S7.

ANALYSIS OF THE STEADY-STATE TIP-COMPLEX RADIUS

The concentration of free CL at the rim of the tip-complex (Eqs.14,18) as a function of the rim's radius ($\rho_f(R_{tip})$) is plotted in Fig.S8 for a range of protrusion heights. In the case where the protrusion is short enough ($h < z_1, |z_2|$) CL can diffuse outside ($J_{out}(0) \neq 0$) and $\rho_f(R_{tip} \to 0)$ is finite. For long protrusions $J_{out}(0) = 0$ and therefore $\rho_f(R_{tip} \to 0)$ can be very large and mathematically it diverges. An immediate conclusion from this behavior is that while it is possible to maintain a long protrusion at any radius, for short protrusion this is not always true and depends on the rates and concentrations of the nucleators and inhibitors. By controlling these parameters the cell can allow only protrusions above certain critical height to survive.

In all cases $\rho_f(R_{tip})$ decays over a length-scale of $\sqrt{D_{tip}/k_{tip}}$ (Fig.S8), and for $R_{tip} \gg \sqrt{D_{tip}/k_{tip}}$, $\rho_f(R_{tip})$ can be considered a constant. This means that for radii that are larger than this value the radius is very sensitive to fluctuations in the concentrations of CL, inhibitors and nucleators. i.e. small fluctuations in those parameters will result in huge changes in R_{tip}, in contrast to observations. We therefore conclude that in biological system one should expect $R_{tip} \ll \sqrt{D_{tip}/k_{tip}}$.

In Fig.S9 we plot the concentration of free CL+myosin complexes (Eqs.16,17), along the length of the protrusion, and at the protrusion tip. Due to the active transport towards the tip, the CL are highly localized at the tip, and their diffusive outflux is significant only when the protrusion height is small.

Analytical approximation for the steady-state radius

In the limit of short ($h \ll z_{1,2}$) and thin ($R_{tip} \ll \sqrt{D_{tip}/k_{tip}}$) protrusions, we can approximate $\rho_f(R_{tip})$ (Eqs.14,18) as

$$\rho_f(R_{tip}) = u_f(h) \simeq u_f(0) + \frac{u_f(0)(2k^u_{on}v_m - k_{tip}k^u_{off}R_{tip})}{2D_u k^u_{off}}h. \tag{S17}$$

Using this approximation in Eq.(21) we get the steady-state relation between the height and the tip radius

$$h_R \simeq \frac{2D_u k^u_{off}[\phi - u_f(0)]}{u_f(0)(2k^u_{on}v_m - k_{tip}k^u_{off}R_{tip})} \tag{S18}$$

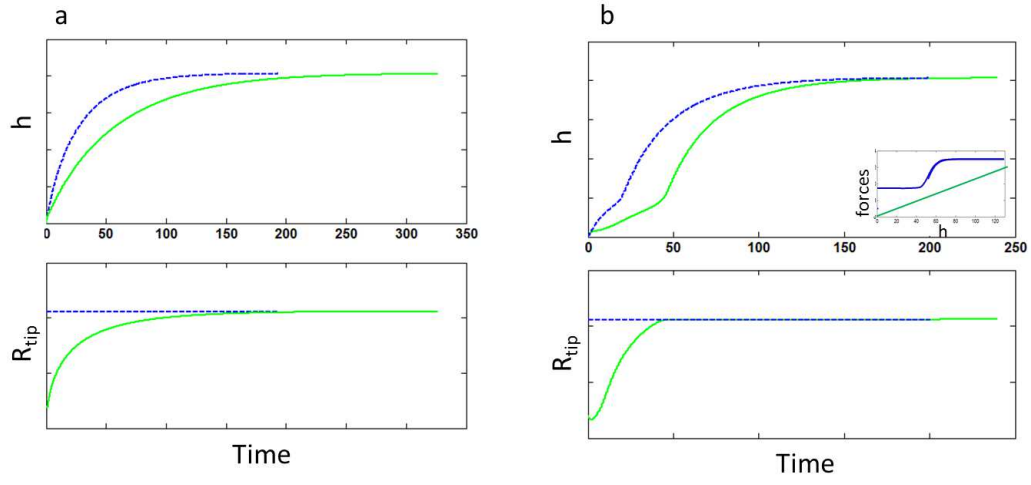

FIG. S3: The dynamics of both the protrusion radius and height as arise from the combination of the force model and the dynamic width regulation model. a) Constant polymerization rate. Dashed blue lines corresponds to the case of a constant radius as in Fig.S2 while solid green lines shows growing radius when $O(\tau_h) = O(\tau_R)$. b) Same as in (a) for height dependent polymerization rate, with the resulting protrusive and restoring forces as shown in the inset (blue and green respectively)..

where $\phi = \eta_{nuc}/k_{on}^{nuc}c_{nuc}$. This relation is plotted in Fig.S10 and is compared to the numerical solution of $R_{tip}(h)$. From (Eq.S18) we find that for short protrusions ($h < z_1, |z_2|$) the maximal radius is given by: $R_{max} = 2k_{on}^{u}v_m/k_{tip}k_{off}^{u}$. The critical height below which there are no solutions of finite radius is given by:

$$h_{min} = \frac{D_u k_{off}^u [\phi - u_f(0)]}{u_f(0) k_{on}^u v_m} \tag{S19}$$

Note that this is independent of k_{tip} and therefore independent of the actin polymerization rate (Eq.14). The increase of the height with the radius above the minimal value is linear, with a slope given by

$$\left.\frac{dh}{dR}\right|_{R=0} = \frac{D_u k_{tip} (k_{off}^u)^2 (\phi - u_f(0))}{2u_f(0)(k_{on}^u)^2 v_m^2} \tag{S20}$$

which increases with the polymerization rate (through k_{tip}, Eq.14). For $h \gg z_1, |z_2|$ the maximal radius is given by approximating (Eq.21) using Eq.(19):

$$R_{max} = \frac{2D_{tip}k_{off}^u \phi}{u_0 k_{on}^u v_m} \left(1 - \sqrt{1 - \frac{2u_0^2 k_{on}^u v_m^2}{\phi^2 (k_{off}^u)^2 D_{tip} k_{tip}}}\right). \tag{S21}$$

The condition for a finite solution is: $2u_0^2 k_{on}^u v_m^2 < \phi^2 (k_{off}^u)^2 D_{tip} k_{tip}$. We should note that comparison between the numeric solution and the analytical approximation for different parameter values reveals that the approximations give rather poor results for the values of h_{min}, $dh_R/dR_{R=0}$ and $R_{max}(h < z_1, |z_2|)$, but do capture correctly the dependencies of h_{min}, $dh_R/dR_{R=0}$ on the polymerization rate. Additionally the computed R_{max} (for $h \gg z_1, |z_2|$) proves to be a very good approximation of its exact value (Fig.S10).

ALTERNATIVE SHAPE MODEL BASED ON MEMBRANE-ACTIN ADHESION

Protrusion height

We demonstrate here another route to formation of protrusions with well defined height, that does not involve the protrusive force of actin polymerization, in contrast to the model explored in the main text. In order to envelope a cylindrical actin bundle by the plasma membrane of the cell, a binding between the membrane and the actin needs to exist in order to counterbalance the bending and stretching energy of the membrane deformation. Since the actin filaments that compose the bundle are continuously treadmilling, due to actin polymerization at their barbed ends (at the protrusion tip) and depolymerization at their pointed ends (at the protrusion base or inside the cytoskeleton bellow the protrusion), any membrane-actin binding protein will get washed out of the protrusion after some time. A binding protein that can diffuse in the membrane when not bound to actin will have a steady-state concentration

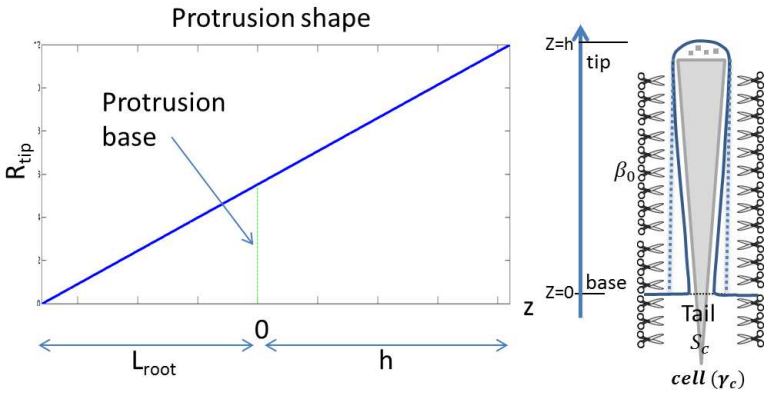

FIG. S4: When the severing is uniform along the entire protrusion the result is an actin bundle with a conical shape, with a slope of A/β. The rootlet length is denoted by L_{root}.

profile that is exponentially decaying from the protrusion base towards its tip [1]. A mechanism of activation of the binding proteins only at the protrusion tip [4] can induce an opposite gradient, having maximal membrane-actin binding at the protrusion tip and decaying towards the base.

Let us write the balance of forces that maintain the steady-state height of a single cylindrical protrusion with radius R in this case, where we ignore the role of actin treadmilling in providing any force. The constant restoring force due to the membrane deformation is given by

$$F_{mem} = 2\pi\left(\kappa\frac{1}{R} + \sigma R\right) \tag{S22}$$

The protrusive force due to membrane-actin binding is given by the derivative of the adhesion energy

$$\begin{aligned} E_{bind} &= -2\pi R\varepsilon_b \int_0^h \rho(z)dz \\ F_{bind} &= -\frac{\partial E_{bind}}{\partial z} = 2\pi R\varepsilon_b\rho(0) \end{aligned} \tag{S23}$$

where ε_b is the average binding energy per unit area (taking into account the relative binding probability of each motor: $k_{off}/(k_{on}+k_{off})$) and $\rho(z)$ is the local density of binding proteins along the protrusion. Eq.S23 simply states the additional energy gained per unit length of membrane annulus that is pulled from the surrounding and attached to the actin bundle, and is therefore dependent on the concentration of binding proteins at the protrusion base $\rho(0)$.

Passive actin-membrane adhesion molecules diffusing from the base

Due to the treadmilling the binding proteins have in general the following distribution [1]

$$\rho(z) = \rho_0 e^{(-zv_a k_{on}/Dk_{off})} \tag{S24}$$

where v_a is the treadmilling velocity, D is the diffusion coefficient of the binding protein when not bound to actin, and k_{on}, k_{off} are the on/off rates for the binding/unbinding to actin.

In this case, since the concentration of binding proteins at the base is constant, $\rho(0) = \rho_0$, we have a constant protrusive force due to the binding proteins. If this constant force is larger than the constant restoring force from the membrane (Eq.S22), the protrusion can grow. However, above a certain height the binding density along the bundle will be too low, and the membrane could decrease its elastic energy by detaching from the actin bundle (see illustration in Fig.S11a).

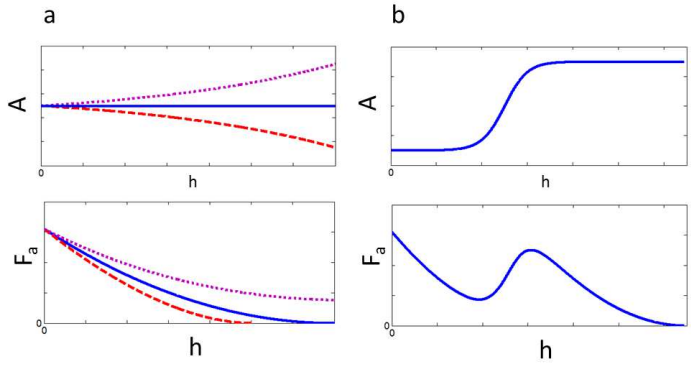

FIG. S5: The protrusive force due to actin (F_a) of a conical protrusion as a function of the height, for different height-dependent polymerization rate ($A(h)$). If the polymerization rate does not increase with h fast enough (condition in Eq.), the rootlet length and therefore the rootlet surface area decreases as the protrusion height increases. The protrusive force will therefore decrease with the decrease of the rootlet (a). If on the other hand the polymerization rate increases strongly enough with height then it compensate for the decrease in the rootlet surface area, resulting in an increase of $F_a(h)$ (b).

Passive actin-membrane adhesion molecules activated at the tip

Recently [4] a mechanism of activating passive actin-membrane adhesion at the protrusion tip was described. In this case the concentration of activated binding proteins decays from the tip towards the base, as the binding proteins are advected by the treadmilling actin and are de-activated at a constant rate α. The distribution becomes (assuming that the rate of production of activated proteins at the tip is constant)

$$\rho(z) = \rho_0 e^{-(h-z)/(v_a/\alpha)} \tag{S25}$$

as illustrated in Fig.S11b.

In the tension dominated regime, equating the restoring force of the membrane (Eq.S22) to the energy of the binding at the base of the protrusion (i.e. location at which the binding becomes too weak to hold the membrane on the actin core), gives the steady-state height

$$h_{ss} = \frac{v_a}{\alpha} Log\left[\frac{\rho_0 \varepsilon_b}{\sigma}\right] \tag{S26}$$

In the curvature-dominated regime the result becomes

$$h_{ss} = \frac{v_a}{\alpha} Log\left[\frac{\rho_0 \varepsilon_b R^2}{\kappa}\right] \tag{S27}$$

This result is interesting:

- The steady-state height is independent of the radius.
- Larger polymerization rate v_a increases the height, while tension σ and ERM-de-activation rate α decrease it.

Protrusion radius

So far the radius of the protrusion R was treated as another free parameter. We now demonstrate that the binding of the membrane to the actin bundle can also select a unique radius. Let us consider a finite surface area of the cell with a constant total number of cortical actin filaments N_T. This situation may be best realized for the brush-border microvilli, which form a uniform and dense array on the cell surface. In this case the number of protrusions is given

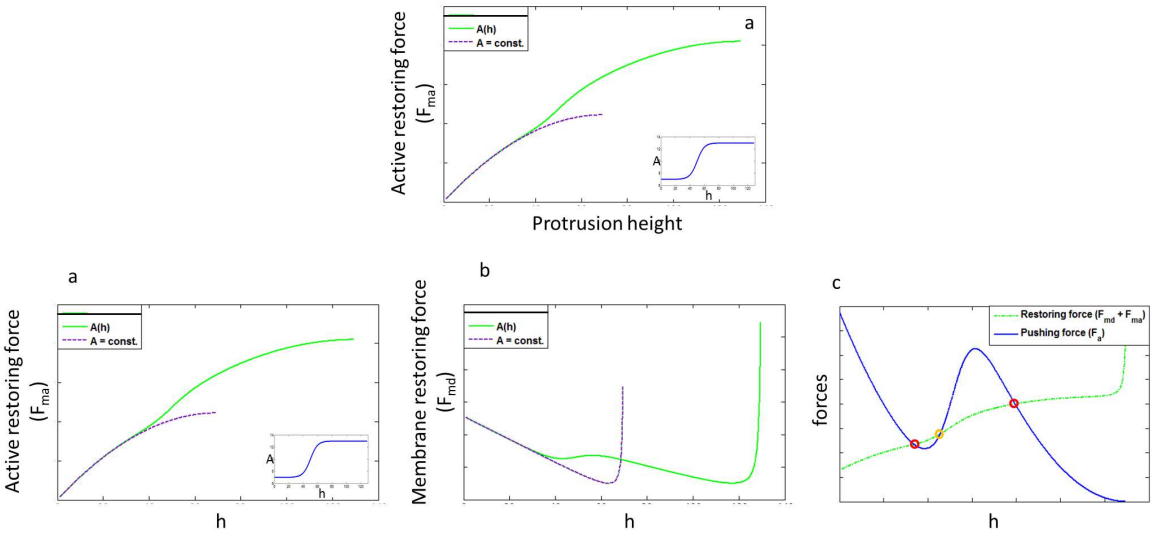

FIG. S6: The restoring force due to membrane-bound myosins (a) and due to the membrane deformation (b). The dashed purple line is for a constant polymerization rate and the solid green line for a polymerization rate that increases with the height $A(h)$ (as shown in the inset). (c) The pushing force (solid blue line) and the sum of all restoring forces (dashed green line). Red circles denote the stable steady-state solutions and the yellow circle the unstable solution.

by: $N_p = N_T a^2/R^2$, where a is the radius of an individual actin filament in the bundle (including the additional width due to adsorbed crosslinkers).

The total binding energy of the actin-membrane system is now (for simplicity consider a uniform distribution of motors along the protrusion: $\rho(z) = \rho_0$)

$$E_{bind} = -2\pi R \varepsilon_b \rho_0 h N_T \frac{a^2}{R^2} \tag{S28}$$

where the negative sign denotes that this is a binding energy. The membrane deformation energy is

$$E_{mem} = 2\pi \left(\kappa \frac{1}{R} + \sigma R \right) h N_T \frac{a^2}{R^2} \tag{S29}$$

Combining these expressions we find the equilibrium radius by taking the derivative to vanish

$$E_{tot} = E_{bind} + E_{mem} = 2\pi h N_T a^2 \left(\frac{\kappa}{R^3} + \frac{\sigma - \varepsilon_b \rho_0}{R} \right) \tag{S30}$$

$$\frac{\partial E_{tot}}{\partial R} = 0, \Rightarrow, R = \sqrt{\frac{3\kappa}{\varepsilon_b \rho_0 - \sigma}} \tag{S31}$$

In the limit that the binding is weak, such that $\varepsilon_b \rho_0/\sigma \to 1$, the width of the protrusion increase and a single protrusion contains all the actin bundles. As the binding strength increases the radius decreases. The cell could control the radius of the protrusions by modifying the density of motors and their affinity to actin.

Such a model would predict that increasing the binding of myosin-I to actin, or its overall concentration, would result in thinner protrusions.

* Corresponding author: nir.gov@weizmann.ac.il

[1] M. Naoz, U. Manor, H. Sakaguchi, B. Kachar, and N.S. Gov. Protein localization by actin treadmilling and molecular motors regulates stereocilia shape and treadmilling rate. *Biophysical journal*, 95(12):5706–5718, 2008.

[2] A.K. Rzadzinska, M.E. Schneider, C. Davies, G.P. Riordan, and B. Kachar. An actin molecular treadmill and myosins maintain stereocilia functional architecture and self-renewal. *The Journal of cell biology*, 164(6):887–897, 2004.

[3] T.M. Svitkina, E.A. Bulanova, O.Y. Chaga, D.M. Vignjevic, S. Kojima, J.M. Vasiliev, and G.G. Borisy. Mechanism of filopodia initiation by reorganization of a dendritic network. *The Journal of cell biology*, 160(3):409–421, 2003.

[4] A. Bretscher Viswanatha, R. and D. Garbett. Dynamics of ezrin and ebp50 in regulating microvilli on the apical aspect of epithelial cells. *Biochemical Society transactions*, 42(1):189–194, 2014.

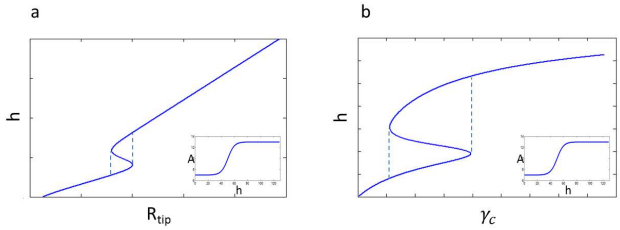

FIG. S7: The steady-state height of the protrusion as a function of the tip radius R_{tip} (a) and the cytoplasm viscosity γ_c (b). In both cases there is a region between the dashed lines in which there are two branches of stable solutions.

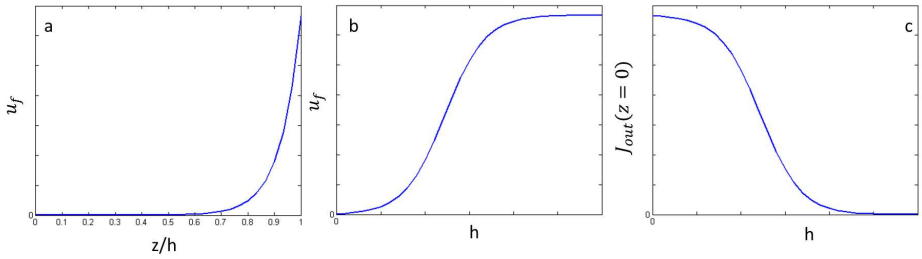

FIG. S9: Calculated steady-state concentration profile of the myosin+CL that are not bound to the actin bundle (u_f, Eqs.16,17) along the protrusion length (a), and as a function of the protrusion height (b) showing that the CL are concentrated close to the tip and that their concentration reaches saturation as a function of the height (due to the incorporation at the tip). (c) The diffusive outflux of CL at the base ($J_{out}(z=0)$). For long protrusions the outflux decreases to zero and the only way for the CL to exit the protrusion is by incorporation to the bundle at the tip.

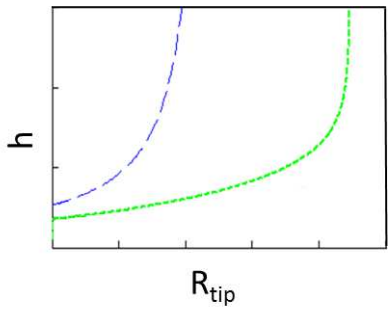

FIG. S10: A comparison between the full numerical solution for the steady-state width of the tip complex $R_{tip}(h)$ (green line, Eq.21) and the simplified analytic solution given in Eq.(S18) (blue line), for a constant polymerization rate.

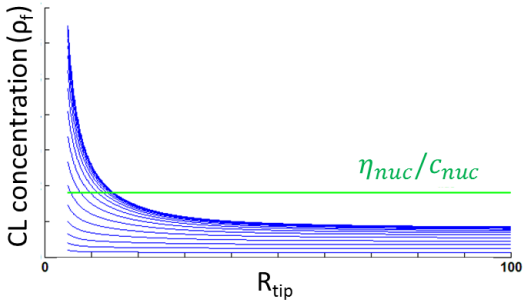

FIG. S8: The steady-state concentration of free CL at the rim of the tip complex as a function of the tip complex radius (Eqs.14,18). The different lines correspond to increasing protrusion heights (in ascending order). An increase in the height decreases J_{out} and therefore increases the CL concentration at the tip. The concentration decays over a length scale of $\sqrt{D_{tip}/k_{tip}}$, and reaches an asymptotic value for large radii. The CL concentration for which a steady-state radius exists is defined by the ratio η_{nuc}/c_{nuc} (Eq.21, horizontal green line). Note that for protrusion heights where the CL concentration is below the green line there are no solutions for any choice of radius.

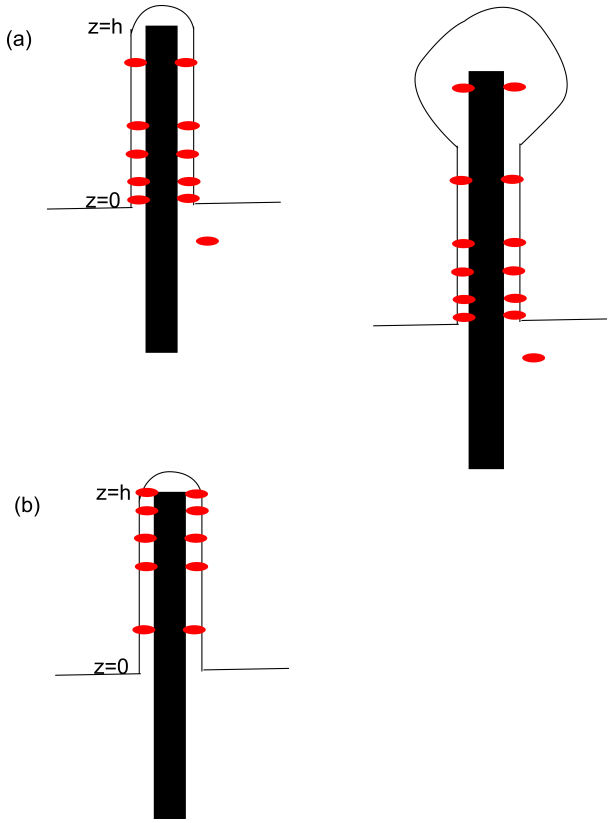

FIG. S11: Illustration of the growth of protrusions driven by membrane-actin binding. (a) If the binding proteins diffuse from the protrusion base, they are depleted from the tip region, which can then detach from the actin core. (b) For binding proteins that get activated at the tip, they are depleted from the protrusion base and this can select the steady-state protrusion height (Eqs.S26,S27).